# Planetary period oscillations in Saturn's magnetosphere: Comparison of magnetic oscillations and SKR modulations in the postequinox interval

G. Provan, L. Lamy, S. Cowley, M. Dougherty

AGU PUBLICATIONS

JGR

Journal of Geophysical Research: Space Physics

RESEARCH ARTICLE
10.1002/2014JA020011

**Key Points:**
- Postequinox magnetic and SKR modulation periods show good general agreement
- South period longer than north by ~3 min from late 2010 to at least mid-2013
- SKR shows effects of ~200 day amplitude/period changes seen in magnetic data

**Correspondence to:**
G. Provan,
gp3@ion.le.ac.uk

**Citation:**
Provan, G., L. Lamy, S. W. H. Cowley, and M. K. Dougherty (2014), Planetary period oscillations in Saturn's magnetosphere: Comparison of magnetic oscillations and SKR modulations in the postequinox interval, *J. Geophys. Res. Space Physics*, *119*, 7380–7401, doi:10.1002/2014JA020011.

Received 24 MAR 2014
Accepted 1 SEP 2014
Accepted article online 3 SEP 2014
Published online 22 SEP 2014



# Planetary period oscillations in Saturn's magnetosphere: Comparison of magnetic oscillations and SKR modulations in the postequinox interval

**G. Provan[1], L. Lamy[2], S. W. H. Cowley[1], and M. K. Dougherty[3]**

[1]Department of Physics and Astronomy, University of Leicester, Leicester, UK, [2]LESIA, Observatoire de Paris, CNRS, UPMC, Université Paris Diderot, Meudon, France, [3]Blackett Laboratory, Imperial College London, London, UK

**Abstract** We compare the properties of planetary period oscillations observed in Saturn kilometric radiation (SKR) and magnetospheric magnetic field data from Saturn equinox in August 2009 to July 2013. As shown previously, the southern and northern oscillation periods converged across equinox from ~10.8 h and ~10.6 h, respectively, during southern summer, to closely common values ~10.7 h approximately 1 year after equinox. Near coalescence is judged to have occurred approximately 3 months earlier in the SKR data, centered in late June 2010, than in the magnetic data, in late September, though SKR periods were particularly difficult to determine during this interval due to less clearly modulated emissions. Both data sets agree, however, that by early November 2010 the two periods had separated again but remained closely spaced with a difference in period of ~3 min about a mean of ~10.67 h, with the southern period remaining longer than the northern. Thus, no enduring reversal of the northern and southern periods took place following near coalescence in mid-2010, the periods remaining uncrossed to the end of the interval studied here. The SKR modulations also show effects related to the sharp amplitude changes observed in the magnetic oscillation data at ~100–200 day intervals since February 2011, though the correspondences are not exact, indicating that other factors such as "seeing" effects on the variable Cassini orbit are also involved. Postequinox variations in the relative phase between the magnetic and SKR oscillations are also shown to be related to changes in orbit apoapsis orientation.

## 1. Introduction

Despite the near-perfect axisymmetry of Saturn's internal planetary magnetic field [e.g., *Burton et al.*, 2010], observations from Pioneer-11, Voyager-1 and Voyager-2, and Cassini have shown that rotating modulations near the ~11 h planetary period are ubiquitous in Saturn's magnetosphere. Such modulations are observed near continuously in the magnetic field, plasma parameters, energetic particle fluxes, and associated neutral atom emissions, as well as auroral ultraviolet, infrared, and radio emissions [e.g., *Warwick et al.*, 1981, 1982; *Desch and Kaiser*, 1981; *Gurnett et al.*, 1981, 2007, 2010a; *Sandel and Broadfoot*, 1981; *Sandel et al.*, 1982; *Carbary and Krimigis*, 1982; *Espinosa and Dougherty*, 2000; *Espinosa et al.*, 2003a, 2003b; *Krupp et al.*, 2005; *Cowley et al.*, 2006; *Kurth et al.*, 2007; *Southwood and Kivelson*, 2007; *Carbary et al.*, 2007, 2008a, 2008b; *Zarka et al.*, 2007; *Andrews et al.*, 2008; *Nichols et al.*, 2008, 2010a, 2010b; *Burch et al.*, 2009; *Provan et al.*, 2009a, 2009b; *Clarke et al.*, 2006, 2010a, 2010b; *Wang et al.*, 2010; *Ye et al.*, 2010; *Badman et al.*, 2012; *Lamy et al.*, 2013]. Cassini observations of modulations in the powerful Saturn kilometric radiation (SKR) emissions have shown that there are in fact two such planetary period oscillation (PPO) systems present, one related to each polar hemisphere, that rotate about the planetary axis with slightly different periods [*Kurth et al.*, 2008; *Gurnett et al.*, 2009a, 2009b]. These periods are also found to vary slowly with Saturn's seasons, being more widely separated during southern summer conditions, ~10.8 h for the southern and ~10.6 h for the northern system, but converging toward ~10.7 h across equinox [*Galopeau and Lecaheux*, 2000; *Gurnett et al.*, 2010b, 2011; *Lamy*, 2011].

The magnetic perturbations for each hemispheric system form a quasi-uniform field within the equatorial quasi-dipolar magnetosphere (typically within dipole $L \approx 15$), closing over the corresponding polar hemisphere in the form of the field of a planet-centered dipole transverse to the planet's magnetic/rotation axis [*Provan et al.*, 2009a, 2011; *Andrews et al.*, 2010a, 2010b]. The perturbations associated with one

hemisphere are found to be excluded from the polar region of the other to within a ~10% limit of experimental determination [*Andrews et al*., 2012]. Each perturbation field pattern rotates around the planet's spin axis at the PPO period corresponding to the system concerned, "beating" within the equatorial region where the two quasi-uniform fields coexist [*Provan et al*., 2011]. These magnetic perturbations are taken to be associated with a corresponding hemispheric rotating current system that flows into the planet's ionosphere along field lines on one side of the planet and out on the other, closing both in the equatorial magnetosphere and in the opposite hemisphere [*Southwood and Kivelson*, 2007; *Andrews et al*., 2010b; *Southwood and Cowley*, 2014]. The SKR emissions are due to cyclotron maser instability of accelerated auroral electron distributions in regions of upward directed field-aligned current [e.g., *Zarka*, 1998; *Lamy et al*., 2010, 2011] that are modulated by the rotating currents of the PPOs [*Southwood and Kivelson*, 2009]. Rotating enhancements of the SKR emissions are thus observed [*Lamy*, 2011; *Andrews et al*., 2011], which should therefore be directly connected with the related magnetic periods through the rotating system of field-aligned currents that generate both.

SKR sources in the postdawn to prenoon sector are much more intense than at other local times [e.g., *Lamy et al*., 2009], however, such that these dominate the emissions observed in the local time (LT) sector spanning dawn from postmidnight to near noon where this beamed radiation can be observed. This leads to strobe-like SKR modulations for observers within this wide LT sector, as deduced from initial Voyager observations [*Desch and Kaiser*, 1981; *Kaiser et al*., 1984]. The dominant sources, centered near ~8 h LT, are suggested to be formed from the interaction between the rotating PPO current system and a quasi-static system associated with the solar wind interaction which produces maximum upward currents in the dawn sector [*Southwood and Kivelson*, 2009]. An SKR burst occurs throughout the dawn sector as the upward current of the PPO system coincides with the dawn sector upward current in the quasi-static system, once per rotation. Observations at other LTs, however, will correspond to PPO-related modulations of more local SKR sources, though skewed toward the more powerful sources in the postdawn sector [*Andrews et al*., 2011; *Lamy*, 2011].

A summary of observational knowledge of the seasonal dependence of the southern and northern PPO periods is shown in Figure 1, where we have combined the results of analyses of SKR data from the Voyager approach interval in 1980 [*Desch and Kaiser*, 1981], Ulysses remote observations during 1993–2002 [*Galopeau and Lecacheux*, 2000; *Gurnett et al*., 2010b], Cassini observations from planetary approach in 2003–2004 (horizontal red bar) [*Gurnett et al*., 2005], and Cassini approach and in-orbit observations from 2004 to mid-2010 [*Lamy*, 2011]. As indicated in Figure 1a, which shows the planetocentric latitude of the Sun at Saturn, the figure thus encompasses slightly more than one Saturn year, from vernal equinox (March 1980) during the Voyager era, through autumnal equinox (November 1995) spanned by the Ulysses data, and southern summer and vernal equinox (August 2009) again during the Cassini era. The PPO periods are shown in Figure 1b, where the southern period is shown by the red data and the northern by the blue, but where the Ulysses data are shown purple, since its hemisphere of origin has not been directly determined from the state of circular polarization of the emission. SKR is emitted mainly in the extraordinary mode, so that the southern and northern emissions are primarily left-hand (LH) and right-hand (RH) polarized, respectively. The Ulysses and Cassini data together indicate a double-peaked period profile for the dominant Southern Hemisphere oscillations during southern summer. The variation of the northern period over this interval is less well determined, but it was evidently significantly smaller than the period of the southern oscillations in the postsummer solstice interval, before the two periods converged toward each other at ~10.7 h over a ~2 year interval spanning equinox as indicated above. The two closely spaced Voyager periods observed near vernal equinox in 1980 are seen to be similar to the near-converged periods observed by Cassini one Saturn year later. Although no polarization-separated analysis was performed on the Voyager radio data, the dominant lower period has reasonably been assigned in Figure 1b to the Northern Hemisphere on the basis of the strongly and exclusively right-hand polarization of the SKR emissions found by *Kaiser et al*. [1980] over a 40 day interval on the northern inbound Voyager passes, though we note that the modulation period analysis reported by *Desch and Kaiser* [1981] employed data over a more extended 267 day interval. The secondary period observed in the latter data has then been more tentatively attributed to the southern period.

It remains unclear from these data, however, whether the southern and northern periods cross postequinox, or whether they approach each other and then diverge again. From comparison with the Cassini data, it seems reasonable to infer that the longer of the diverged Ulysses periods postautumnal equinox (1997–2002)

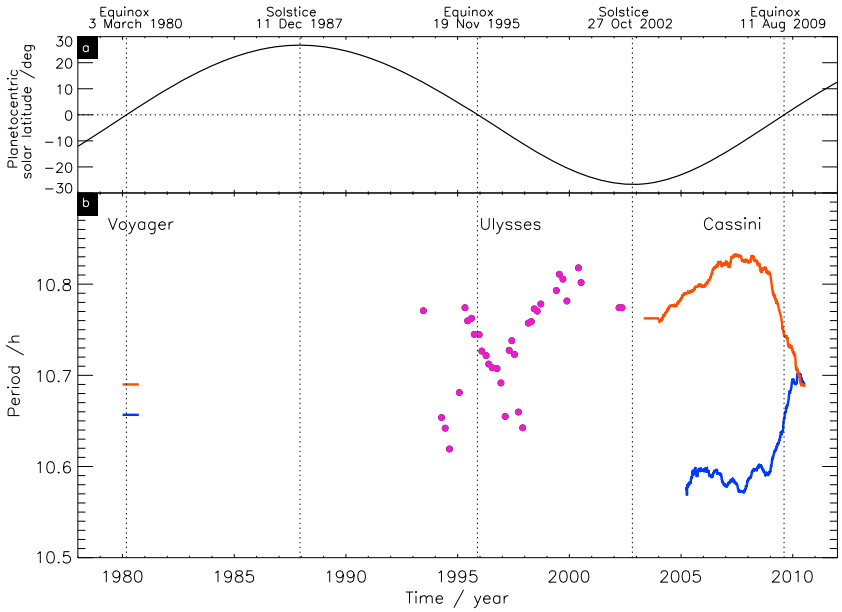


**Figure 1.** Plot showing (a) the planetocentric latitude of the Sun at Saturn and (b) the PPO rotation periods derived from SKR data from Voyager, Ulysses, and Cassini measurements as indicated, over a ~31 year interval spanning more than a full Saturn year (for sources, see citations in section 1). The southern and northern periods determined from Voyager and Cassini SKR data are shown by the red and blue lines, respectively, while those from Ulysses data are shown by purple dots since the corresponding hemisphere of emission remains undetermined from measurement of the polarization. The emissions observed by Voyager were principally RH polarized (northern), such that their principal modulation period is taken to correspond to the northern period (blue line), in close agreement with the Cassini period one Saturn year later, while the secondary period is attributed with somewhat less certainty to the southern period (red line). The vertical dotted lines indicate Saturn's seasons, specifically the northern and southern summer solstices where the solar latitude in Figure 1a is maximum and minimum, respectively, and the equinoxes where the latitude passes through zero. The dates of these events are given at the top of the plot.

corresponds to the Southern Hemisphere and the shorter to the northern, as implied above. However, we do not know directly which of the diverged periods observed by Ulysses preautumnal equinox (1993–1995) belong to which hemisphere. On the basis of the source hemispheres indicated by the concurrent Saturn latitude of the spacecraft, *Gurnett et al.* [2010b] suggested that the southern and northern periods crossed in the postequinox Ulysses interval and further suggested from study of a slightly extended SKR data set compared with Figure 1b that a related reversal took place in the opposite sense in the postequinox Cassini data [*Gurnett et al.*, 2011]. However, a study of the postequinox oscillations in Cassini magnetic field data by *Provan et al.* [2013] indicates the occurrence of an extended interval of closely spaced periods unlike the postequinox Ulysses data, with the southern period remaining somewhat longer than the northern, at least to the end of 2012. Here we therefore examine and compare the magnetic field and SKR oscillations in the postequinox interval, extending both data sets to mid-2013.

## 2. Comparison of Magnetic Field and SKR PPO Properties: Previous Results

Unlike the SKR modulations which can be observed remotely from the planet, magnetic oscillation data can only be determined in situ within Saturn's magnetosphere, and thus exist (apart from short segments of Voyager and Pioneer-11 data) only for the in-orbit Cassini era, beginning mid-2004 [*Andrews et al.*, 2008, 2010a, 2010b, 2012; *Provan et al.*, 2009a, 2011, 2012, 2013]. Following initial studies by *Andrews et al.* [2010b] and *Southwood* [2011], *Andrews et al.* [2012] presented a comparison between magnetic and SKR oscillation periods extending to early 2011 in the postequinox interval. This comparison is summarized in Figure 2, which shows Cassini orbital and PPO data over the interval $t = 172 - 2597$ days, where $t = 0$ corresponds to 00 UT on 1 January 2004, thus spanning 21 June 2004 to 9 February 2011 inclusive. The figure focuses specifically on the SKR modulation analysis presented by *Lamy* [2011], though we note that the related results derived independently by *Gurnett et al.* [2011] show very similar behavior [*Andrews et al.*, 2012].

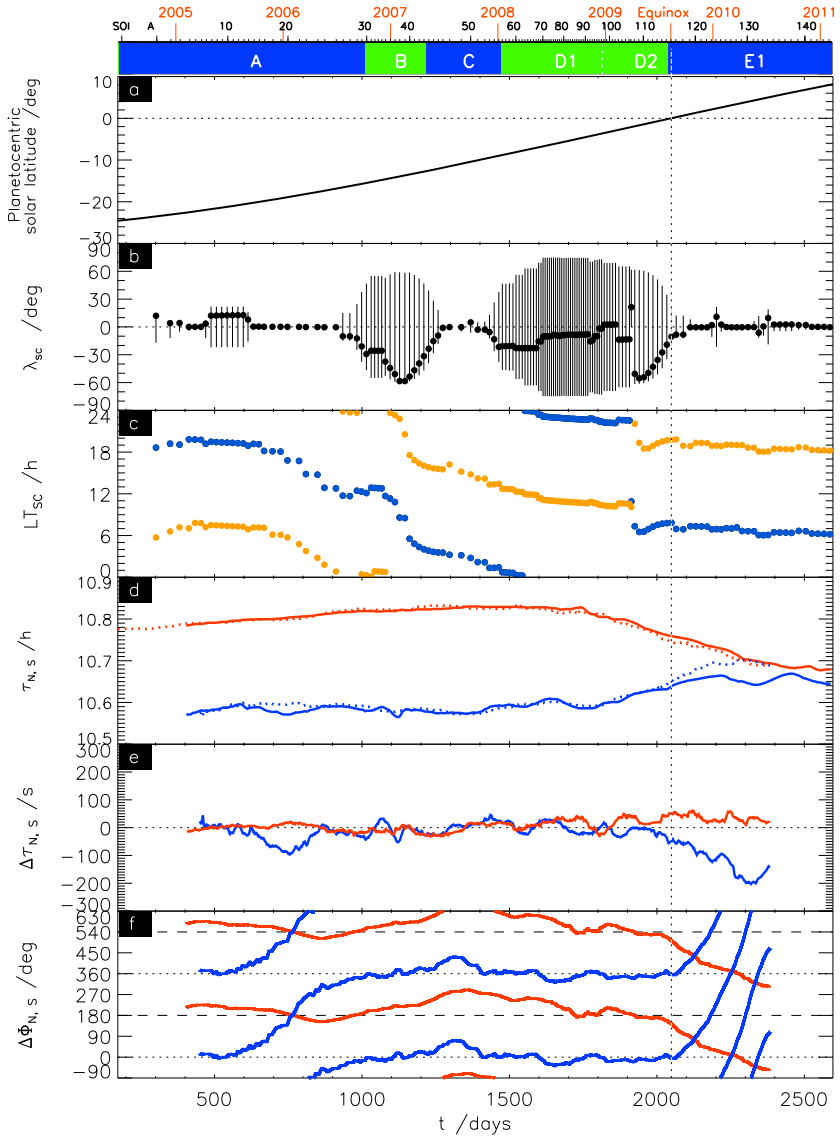


**Figure 2.** Plot showing Cassini orbital parameters and PPO data for the interval $t = 172 - 2597$ days, where $t = 0$ corresponds to 00 UT on 1 January 2004, thus spanning 21 June 2004 to 9 February 2011 inclusive. Start-of-year markers are shown at the top of the plot (red), together with Cassini Rev markers (black) plotted at each periapsis and numbered every 10 Revs and interval identifiers consisting of near-equatorial orbits (blue bars) and highly inclined orbits (green bars), respectively. (a) The planetocentric latitude of the Sun at Saturn, as in Figure 1a, where vernal equinox (11 August 2009) is marked by a vertical dotted line, (b) the latitude of spacecraft periapsis (degrees) for each Rev (black dots) plotted at the time of periapsis, together with the latitude range on that Rev (vertical bars), (c) the LT of periapsis (blue dots) and apoapsis (orange dots) for each Rev, (d) the periods (hours) of the southern (red line) and northern (blue line) magnetic oscillations ($\tau_{Mag\ N,S}$) determined by *Andrews et al.* [2012], together with the periods of the southern (red dots) and northern (blue dots) SKR modulations ($\tau_{SKR\ N,S}$) determined by *Lamy* [2011], (e) the difference (seconds) between the southern (red) and northern (blue) magnetic and SKR periods, $\Delta\tau_{N,S} = \tau_{Mag\ N,S} - \tau_{SKR\ N,S}$, and (f) the difference between the southern (red) and northern (blue) magnetic and SKR phases (degrees), defined as $\Delta\Phi_{N,S} = \Phi_{Mag\ N,S} - \Phi_{SKR\ N,S}$, where two cycles of phase are shown on the vertical axis, with each data point being plotted twice.

The top bar of Figure 2 shows start-of-year markers (red) and Cassini revolution (Rev) numbers (black), the latter defined from apoapsis to apoapsis and plotted here at the time of periapsis. Figure 2a shows the planetocentric latitude of the Sun at Saturn, as in Figure 1a, where vernal equinox is marked by the vertical dotted line. Figure 2b shows the latitude of spacecraft periapsis (degrees) for each Rev (black dots), plotted at the time of periapsis, together with the latitude range of each Rev (vertical bars). This shows a sequence of near-equatorial and highly inclined orbits, which is significant for the nature of the magnetic

oscillation data available for analysis. For near-equatorial orbits, magnetic oscillation properties are obtained from extended (few day) passes through the quasi-dipolar "core" region of the magnetosphere, taken to correspond to dipole $L \leq 12$. For sufficiently inclined orbits, however, data from both northern and southern polar regions are also potentially available, while core region data can be extracted from short periapsis intervals as the spacecraft passes across the equatorial plane, provided that periapsis lies at small enough radial distance [*Andrews et al*., 2010b, 2012]. Intervals of these two orbit types are distinguished by blue and green bars at the top of the figure, plus letter identifiers, where intervals "A," "C," and "E" identify near-equatorial Revs (blue bars), while intervals "B" and "D" identify high-latitude Revs (green bars). In Figure 2c we plot the LT of apoapsis (orange dots) and periapsis (blue dots) for each Rev, showing that a sharp change took place before equinox in early 2009 via an interval of near-circular orbits centered near Rev 107. After this time, apoapsis was located for an extended interval in the dusk sector for the first time in the mission, with consequences for the observability of the otherwise dominant postdawn SKR sources discussed in section 1. The analysis presented by *Andrews et al*. [2011] (their Figure 5) shows that the dusk sources are expected to have become dominant after Rev 112, about 60 days before equinox.

In Figure 2d we present the periods (hours) of the northern (N, blue line) and southern (S, red line) magnetic oscillations ($\tau_{\text{Mag N,S}}$), together with the northern (blue dots) and southern (red dots) SKR periods ($\tau_{\text{SKR N,S}}$) shown previously in Figure 1. Figure 2e shows their difference (seconds), $\Delta\tau_{\text{N,S}} = \tau_{\text{Mag N,S}} - \tau_{\text{SKR N,S}}$, the blue line for the northern periods and the red line for the southern. As shown by *Andrews et al*. [2012], excellent general agreement is found between the periods of the magnetic and SKR PPOs, the differences varying about zero through only a few tens of seconds (i.e., at the ~0.1% level), in accordance with physical expectations outlined in section 1. However, for the southern oscillations we see that starting near the beginning of 2009, and continuing to the end of the joint data set in mid-2010, $\tau_{\text{Mag S}}$ becomes continuously slightly larger than $\tau_{\text{SKR S}}$ by ~30 s, an effect attributed by *Andrews et al*. [2012] to the change in the LT of apoapsis of Cassini's orbit.

The rationale is shown in Figure 2f, where we present the difference between the northern (blue) and southern (red) magnetic ($\Phi_{\text{Mag N,S}}$) and SKR ($\Phi_{\text{SKR N,S}}$) phases (degrees), defined as $\Delta\Phi_{\text{N,S}} = \Phi_{\text{Mag N,S}} - \Phi_{\text{SKR N,S}}$, where we plot two cycles of phase on the vertical axis to emphasize the continuity of the data, with every point being plotted twice. As discussed further in the next section, $\Phi_{\text{Mag N,S}}$ gives the azimuth $\varphi$ of the near-equatorial quasi-uniform magnetic field of the northern or southern system, where $\phi = 0°$ corresponds to the noon meridian (sunward), increasing in the sense of planetary rotation, while the absolute value of $\Phi_{\text{SKR N,S}}$ is such that SKR maxima occur for $\Phi_{\text{SKR N,S}} = 360\ N$ deg, for successive integer values of $N$. The value of their difference (modulo 360°) thus gives the azimuth of the quasi-uniform field at the time of SKR maxima for the corresponding hemisphere. For the southern system this azimuth generally corresponds to the postmidnight sector as deduced by *Andrews et al*. [2008] and *Provan et al*. [2009a], such that the corresponding upward field-aligned currents in the Southern Hemisphere are centered postdawn at times of southern SKR maxima, as discussed in section 1. However, the difference in period noted above causes the relative phase to drift via midnight and dusk to a near-noon position at the end of the joint data, such that the quasi-uniform field then points in almost the opposite direction at southern SKR maxima, with the upward current thus being centered in the dusk sector at these times. As *Andrews et al*. [2011] showed, this is the configuration expected if the SKR sources observed at those times are those in the dusk sector, associated with the dusk LT of spacecraft apoapsis, approximately in antiphase with the sources at dawn. A weaker secondary maximum in SKR emission intensity is indeed centered predusk near ~17 LT [*Lamy et al*., 2009], potentially leading to clear SKR modulation for observers located in the dusk sector. The gradual variation of the southern phase difference in Figure 2f compared with the sharp change in apoapsis LT in Figure 2c results from the combined effect of the varying nature of the spacecraft orbit noted above and the running ~200 day data intervals employed to determine the PPO periods from both magnetic and SKR data sets [*Andrews et al*., 2011, 2012; *Lamy*, 2011].

For the northern system in Figure 2e we see that during the first interval of equatorial orbits, (interval A) a significant deviation between the magnetic and SKR periods occurs, peaking at $\sim -100$ s, centered near $t \approx 750$ days (early 2006). Figure 2f shows that this deviation is associated with a relative rotation of ~360° in the northern phase. Both before and after this deviation, the difference between the northern magnetic and SKR phases varies about zero, such that the northern system quasi-uniform field points sunward at

Northern Hemisphere SKR maxima, as first deduced by *Provan et al*. [2011], implying that the upward currents in the Northern Hemisphere are then centered near dawn, similar to the case of the southern system at southern SKR maxima. *Andrews et al*. [2012] concluded that this effect was caused by a loss of phase lock between the magnetic and SKR phases, due to the very noisy northern magnetic phases during this interval, which overall resulted in the relative loss of one northern period rotation (out of ~700) during this interval. This phase jump is then spread across ~400 days due to the ~200 day data segments employed in the analysis as indicated above.

More importantly, however, a major difference in the northern periods is observed to commence just prior to vernal equinox in 2009, with the deviation peaking at $\sim -200$ s near $t \approx 2300$ days (first half of 2010). The phase difference in Figure 2f rotates over more than two full cycles, in the opposite sense to the phase difference for the southern system. This variation cannot therefore be attributed to the apoapsis LT effect that produces much smaller phase differences in the Southern Hemisphere data. The overall effect is that while the converging southern and northern SKR periods first reach near-equal values in early April 2010 ($t \approx 2290$ days) and remain so for a number of months, the magnetic periods instead come to near convergence in late September 2010 (near $t \approx 2460$ days) and then slightly diverge again without crossing. While the origin of this unexpected difference in the times of near convergence in periods is not wholly clear, we note that determination of the SKR periods was particularly difficult at this time, due to somewhat less clearly modulated signals. The evidence for the behavior in the magnetic data comes directly from the beat effects of the combined oscillations in both amplitude and phase observed within the core region [see *Andrews et al*., 2012, Figure 11].

## 3. Comparison of Magnetic Field and SKR PPO Properties: Postequinox Interval

### 3.1. Magnetic Oscillations in the Postequinox Interval

In this section we extend the magnetic field-SKR comparison into the postequinox northern spring interval and begin by considering the magnetic field data. These have been discussed by *Provan et al*. [2013] to late 2012 and are summarized here in Figure 3 over an extended interval $t = 1827 - 3510$ days, corresponding to 1 January 2009 to 10 August 2013 inclusive. As in Figure 2, Figures 3a–3c show the planetocentric latitude of the Sun at Saturn, the periapsis latitude and latitude range of the Cassini Revs, and the LT of apoapsis and periapsis, respectively. The time of vernal equinox, when the latitude of the Sun passes through zero in Figure 3a, is indicated by the vertical dotted line on the left of the plot. Figure 3b shows that the Cassini orbits during the central part of the interval were near equatorial, intervals E1 to E4 indicated by the blue bar at the top of the figure, bounded on each side by an interval of strongly inclined orbits, interval D2 prior to the equatorial orbits, and F1 and F2 after, shown by the green bars. Figure 3c shows that the LT of periapsis evolved slowly over the interval between postdawn (~7 h LT) and postmidnight (~2 h LT), while apoapsis correspondingly evolved from postdusk (~19 h LT) to postnoon (~14 h LT).

As indicated in section 2, for the equatorial orbits, magnetic oscillation amplitude and phase data are obtained from each periapsis pass through the core region (dipole $L \leq 12$) from fits to suitably filtered residual magnetic field data. The residual field is obtained by subtracting the Cassini Saturn Orbit Insertion internal field model [*Dougherty et al*., 2005], though any recent model would produce essentially identical results, which is then band pass filtered between 5 and 20 h using a standard Lanzcos filter. Spherical polar field components referenced to Saturn's magnetic/spin axis are employed throughout. For the high-latitude orbits, similar data are obtained in the polar regions of both hemispheres from similarly filtered residual field data. As also indicated in section 2, for some high-latitude Revs, it is also possible to obtain core region data of greater uncertainty from fits to short segments of unfiltered magnetic field data, provided the spacecraft periapsis lies sufficiently within the core region [*Andrews et al*., 2010b]. Such data were obtained from intervals F1 and F2, but not from D2, for which the latter condition was not satisfied. For these core intervals only data from the azimuthal ($\varphi$) field component is employed, since the PPO field dominates that component within the core, while the variations in the radial ($r$) and colatitudinal ($\theta$) components are strongly affected by spacecraft passage through the perturbation fields of the quasi-static ring current.

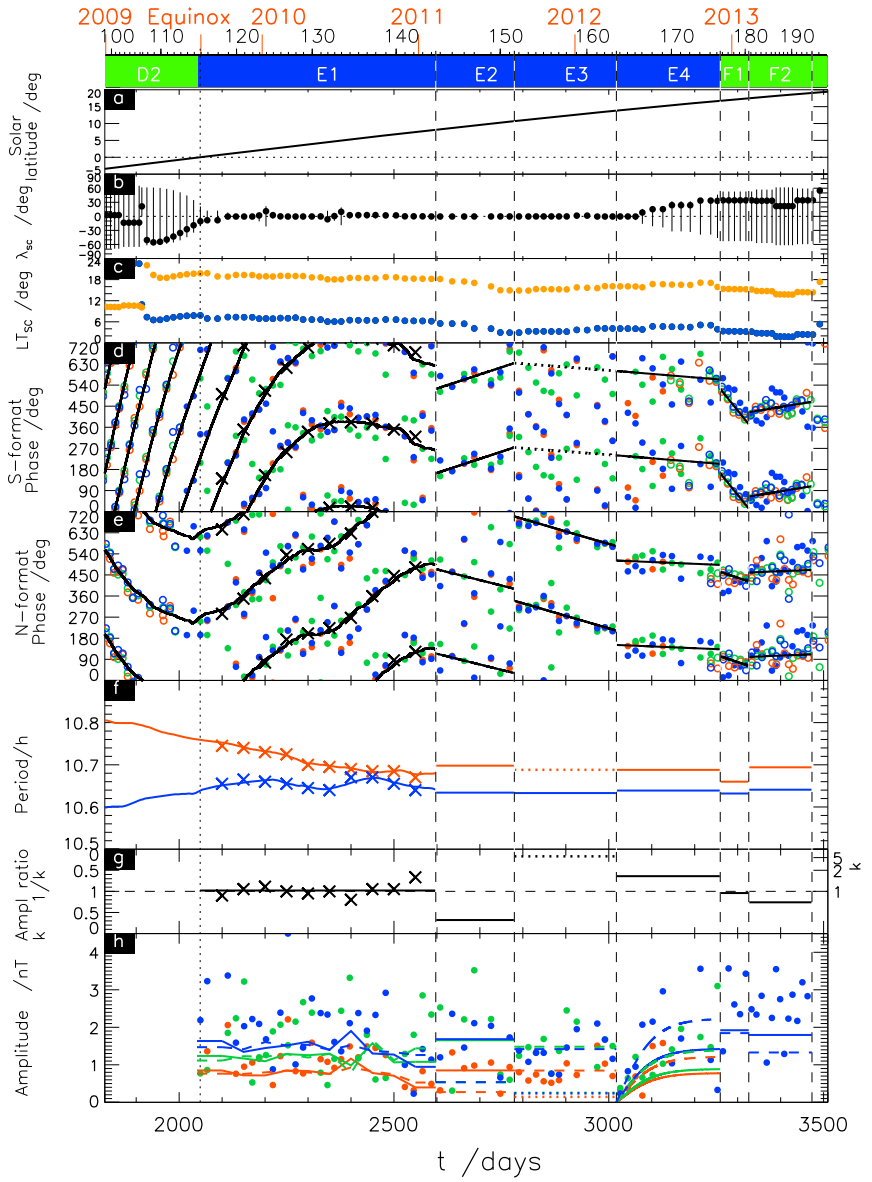


**Figure 3.** Plot showing Cassini orbital parameters and PPO characteristics derived from magnetic field data over the equinoctial and post-equinox interval, $t = 1827 - 3510$ days, spanning 1 Jan 2009 to 10 August 2013 inclusive. Start-of-year and Cassini Rev markers are shown at the top of the plot, together with interval identifiers, in a similar format to Figure 2. The vertical dotted line shows the time of vernal equinox as indicated, while the vertical dashed lines mark the times of six rapid transitions in the magnetic oscillation properties, defining subintervals E1–E4 and F1 and F2. As in Figure 2 the following are shown: (a) The planetocentric latitude of the Sun at Saturn, (b) the latitude of spacecraft periapsis (degrees) for each Rev (black dots) plotted at the time of periapsis, together with the latitude range on that Rev (vertical bars), and (c) the LT of periapsis (blue dots) and apoapsis (orange dots) for each Rev. (d) Magnetic oscillation phase data, $\psi_i$, for field component $i$, plotted in southern format (see text, section 3.1), relative to a core region guide phase corresponding to a fixed period of 10.69 h (equations (1) and (2)). Red, green, and blue data correspond to the $r$, $\theta$, and $\varphi$ field components, respectively, while solid circles indicate phases derived from core region data and open circles indicate phases derived from southern polar magnetic field data. (e) Magnetic oscillation phase data plotted in northern format (see text, section 3.1), relative to a core region guide phase corresponding to a fixed period of 10.64 h, where solid circles indicate phases derived from the same core region phase data as in Figure 2d and open circles indicate phases derived from northern polar magnetic field data. Two full cycles of phase are plotted on the vertical axis of Figures 3d and 3e, with each data point being plotted twice. The black lines and crosses in Figures 3d and 3e show determinations of the southern and northern PPO phases, respectively, based on fits to these data (see the text, section 3.1). The dotted black line in Figure 3d for interval E3 has been interpolated between the end of E2 and the beginning of E4. (f) The rotation periods corresponding to the gradients of these lines (equations (3a) and (3b)), for the southern (red lines and crosses) and northern (blue lines and crosses) oscillation systems. (g) The north/south magnetic oscillation amplitude ratio $k$ determined from the variation of the core region phase data about the fitted lines in Figures 3d and 3e (see text, section 3.1), where in the lower half of the panel the scale is linear in $k$ from zero to unity, while in the upper half it is linear in $1/k$ between unity and zero (corresponding to $k$ values between unity and infinity as indicated on the right side of the panel). (h) The core region magnetic oscillation amplitude data color coded as in Figures 3d and 3e, together with the individual southern (solid lines and dotted line for E3) and northern (dashed lines) oscillation amplitudes obtained from fitting a beat-modulated amplitude model to these data (see text, section 3.1). The values in interval E1 are based on the data indicated by the crosses in Figures 3d–3g. The $\varphi$-component values for F1 and F2 were obtained from short segments of unfiltered core region data obtained on highly inclined orbits.

In all cases, the oscillation amplitude and phase are obtained by fitting the magnetic data for field component $i$ (i.e., spherical polar $r$, $\theta$, or $\varphi$) to an "$m = 1$" rotating perturbation (varying as $e^{-jm\varphi}$) of the form

$$B_i(\varphi, r, t) = B_{0i} \cos\left(\Phi'_g(r,t) - \varphi - \psi_i\right), \quad (1)$$

where, as above, $\varphi$ is azimuth measured from noon, $t$ is time since 00 UT on 1 January 2004, and $r$ is radial distance from the planet. Function $\Phi'_g(r,t)$ is a "guide" phase function that in previous related works [e.g., *Andrews et al*., 2012; *Provan et al*., 2013] has simply been taken to correspond to the phase of an oscillation of fixed period $\tau_g$, close to that of the oscillation of interest. Here, however, in order to include polar data obtained at significantly large down tail radial distance from the later $F$ intervals of the mission (to a maximum here of ~25 $R_S$ for Rev 191), we have also included a radial phase delay such that

$$\Phi'_g(r,t) = \frac{360\ t}{\tau_g}\ \text{deg} \qquad \text{if} \qquad r \le 12\ R_S, \quad (2a)$$

$$\Phi'_g(r,t) = \frac{360\ t}{\tau_g} - G\ (r - 12\ R_S)\ \text{deg} \qquad \text{if} \qquad r \ge 12\ R_S, \quad (2b)$$

where $G$ is the radial phase gradient. The latter value has been investigated by *Arridge et al*. [2011] and *Provan et al*. [2012] with values typically in the range ~2.5 to ~4.5 deg $R_S^{-1}$. For simplicity here we have taken a fixed value $G = 3$ deg $R_S^{-1}$. We note from equations (2a) and (2b) that this does not affect phase values within the core region, for dipole $L \le 12$ but only values from data at larger distances in the tail.

A least squares fit of equation (1) to appropriately selected segments of the (usually) filtered residual magnetic data yields the amplitude $B_{0i}$ and relative phase $\psi_i$ for each field component $i$ for a given Rev, from which the oscillation period can be determined from the pass-to-pass time variation of the relative phase. In Figure 3d these phases are shown in "southern format" (see below) relative to a core guide phase (equations (2a) and (2b)) with a fixed period of 10.69 h, while in Figure 3e the phases are shown in "northern format" (also below) relative to a core guide phase with a fixed period of 10.64 h. The solid symbols ($r$ red, $\theta$ green, and $\varphi$ blue) show the same core region phase data in the two formats, while the open symbols show the polar phase data (when available) from the corresponding hemisphere only. Two cycles of phase are shown on the vertical axis to emphasize the continuity of the data, with each data point being plotted twice. Uncertainties in these relative phases are difficult to robustly assign on an individual basis, but empirical determinations indicate typical values of ~ ±10° [e.g., *Andrews et al*., 2012].

In southern format the relative phases $\psi_i$ are plotted such that for a pure southern oscillation the values for all field components would lie on a common line. Specifically, the $r$ component phase is plotted as measured, the $\theta$ component in phase with $r$ is also plotted as measured, while the $\varphi$ component in lagging (leading) quadrature with $r$ in the core (polar) region is shifted by −90° (+90°) [*Andrews et al*., 2012; *Provan et al*., 2013]. These are the polarization characteristics of a quasi-uniform field within the core region and a related quasi-dipolar field in the southern polar region, as discussed in section 1. Similarly, in northern format the relative phases are plotted such that for a pure northern oscillation the values for all field components would again lie on a common line. Specifically, the $r$ component phase is again plotted as measured, the $\theta$ component now in antiphase with $r$ is shifted by 180°, while the $\varphi$ component again in lagging (leading) quadrature with $r$ in the core (polar) region is shifted by −90° (+90°). These are again the polarization characteristics of a quasi-uniform field within the core region and a related quasi-dipolar field in the northern polar region.

The southern and northern polar phases (open circles) in Figures 3d and 3e, respectively, are indeed seen to be brought to closely common values by this procedure, generally to within a few tens of degrees, confirming the above characteristics of the polar oscillations. *Andrews et al*. [2012] previously showed from analysis of such data that the polar oscillations are pure "southern" and "northern" in the two hemispheres, within an uncertainty limit of ~10% by relative amplitude, as indicated in section 1. However, the core region data (solid circles) in Figures 3d and 3e have been shown to correspond to a superposition of southern and northern oscillations with the above polarization characteristics, whose relative amplitude varies with time [*Provan et al*., 2011, 2013; *Andrews et al*., 2012]. For equal amplitudes, the phase data in both southern and northern formats vary at the beat period of the two oscillations by ±90° about the southern and northern phases (relative to the guide phases), respectively. The individual southern and northern magnetic phases can then be determined from fits

to the banded phase data in southern and northern formats, respectively. For unequal amplitudes, the phase data corresponding to the stronger signal become more closely banded about their hemispheric phase, while the phase data corresponding to the weaker signal become less closely banded about the other hemispheric phase, in general, still allowing the two hemispheric phases to be determined. In the limit that one signal is much stronger than the other, however, the phases corresponding to the strong signal become very closely banded about their hemispheric phase (as for the polar data), while the phase data corresponding to the weak signal become unbanded, such that the oscillation phase of the corresponding hemisphere cannot then be determined. The practical limit on the amplitude ratio within which both hemispheric phases can be discerned for the phase data examined here is a factor ~5 [*Provan et al.*, 2013].

Within this limit, suitable fits to the southern and northern format relative phase data (see below) thus allow determination of the time variation of the relative phase of the $r$ component field oscillations for the two systems, $\psi_{r\ \mathrm{N,S}}(t)$ (the phases of the other two components then following from the above polarization characteristics). The periods of the corresponding oscillations are then determined from the overall phase gradient, taking account of the guide phase

$$\tau_{\mathrm{N,S}}(t) = \frac{360}{\left(\frac{\mathrm{d}}{\mathrm{d}t}\Phi_{\mathrm{N,S}}(t)\right)}, \tag{3a}$$

where

$$\Phi_{\mathrm{N,S}}(t) = \frac{360\ \ t}{\tau_{g\ \mathrm{N,S}}} - \psi_{r\ \mathrm{N,S}}(t)\ \mathrm{deg}. \tag{3b}$$

The amplitude ratio $k$ of the northern and southern oscillations, $k = B_{0\mathrm{i}\ \mathrm{N}}/B_{0\mathrm{i}\ \mathrm{S}}$, assumed the same for all three field components at a given time, can also be determined from the beat period variations of the core region phases about the southern and northern phase lines, or equivalently from the modulation of the phase differences between the ($r$, $\varphi$) and $\theta$ field component oscillations [*Andrews et al.*, 2012; *Provan et al.*, 2013]. Knowing this ratio and the two phases, the core region oscillation amplitudes for each field component of the two systems can then be determined from a fit to the beat-modulated core region amplitude data.

The black lines in Figures 3d and 3e in intervals D2 and E1 show the southern and northern phases (relative to the respective guide phases) determined by *Andrews et al.* [2012] from running 25-point linear fits to the phase data, each fit spanning ~200 days. The fits are made using "directional statistics" methods appropriate to circular measures such as phase angles [*Mardia and Jupp*, 2000]. Figure 3f shows the corresponding oscillation periods for the southern (red line) and northern (blue line) systems, determined from equations (3a) and (3b), as shown in the corresponding interval in Figure 2d. Figure 3g shows the corresponding amplitude ratio $k$ (solid line close to unity in E1, not determined in D2 due to the lack of core region data). The crosses in Figures 3d–3g in interval E1 also show simultaneous five-parameter fits (two linear phases and $k$) to 150 day segments of phase data evaluated every 50 days, showing essentially similar results [*Provan et al.*, 2013]. The amplitude data corresponding to the latter fits are shown in Figure 3h for the southern (solid lines) and northern (dashed lines), respectively, color coded for each field component as for the phase data. These results exhibit the essential continuity of the oscillation phase over the equinoctial and initial postequinox interval, associated with PPO periods that slowly converge to a near-common value near $t \approx 2460$ days (late September 2010) before slightly diverging again in the same sense as before at the end of E1 (as also shown in Figure 2). The relative phase data in E1 also show approximate equal banding ~ ±90° about the fitted lines in southern and northern formats, indicative of $k \approx 1$ during this interval, as seen in Figure 3g.

After this initial interval, however, we observe a change in behavior of the oscillations, with the phase values in southern and northern formats undergoing a series of abrupt changes in slope (i.e., oscillation period) and banding (i.e., amplitude ratio), together with apparent small jumps in phase by up to a few tens of degrees. These changes are marked by the series of vertical dashed lines at intervals of ~100–200 days. Due to the short time intervals involved, only single linear fits to these piecewise segments of phase data have been determined, shown by the straight black lines in Figures 3d and 3e, corresponding to the fixed oscillation periods shown in Figure 3f. The slopes indicate small changes in period about the 10.69 h guide period for the southern oscillations and the 10.64 h guide period for the northern oscillations, thus with the southern period continuing longer than the northern by ~3 min, though with a notable dip in both periods and a narrowing of their difference during interval F1. For ease of reference, these periods and their

**Table 1.** PPO Properties Determined From Magnetic Field and SKR Data

| Interval | Start-End Time (days)[a] Rev Numbers | N/S[b] Magnetic Amplitude Ratio $k$ | N magnitude Period (h) | S Magnitude Period (h) | S-N Magnitude Period Difference (min) | N SKR (RH) Period (h) | S SKR (LH) Period (h) |
|---|---|---|---|---|---|---|---|
| E2 | 2597–2780<br>145–151 | $0.32 \pm 0.07$[c] | $10.634 \pm 0.005$[d] | $10.698 \pm 0.003$[d] | $3.8 \pm 0.3$ | $10.626 \pm 0.014$[e] | $10.693 \pm 0.019$[e] |
| E3 | 2780–3018<br>152–163 | $6$[f] $\pm 2$ | $10.633 \pm 0.002$ | $10.688$[g] | $3.3$[g] | $10.633 \pm 0.010$ | - |
| E4 | 3018–3259<br>164–175 | $1.56 \pm 0.29$ | $10.639 \pm 0.002$ | $10.688 \pm 0.004$ | $2.9 \pm 0.3$ | - | $10.681 \pm 0.010$ |
| F1 | 3259–3326<br>176–180 | $0.96 \pm 0.19$ | $10.632 \pm 0.004$ | $10.660 \pm 0.003$ | $1.7 \pm 0.3$ | - | $10.657 \pm 0.062$ |
| F2 | 3326–3473<br>181–194 | $0.74 \pm 0.23$ | $10.641 \pm 0.002$ | $10.694 \pm 0.001$ | $3.2 \pm 0.1$ | $10.641 \pm 0.015$ | $10.688 \pm 0.017$ |

[a]Time $t = 0$ corresponds to 00 UT to 1 January 2004.
[b]N and S in the table refer to the northern and southern oscillatory systems, respectively.
[c]Uncertainty estimated as in *Provan et al.* [2013].
[d]Determined from the uncertainty in the gradient of the linear fit to the S- and N-format magnetic phase data, as in *Provan et al.* [2013].
[e]Determined from the FWHM of the Lomb-Scargle periodogram.
[f]Derived from a fit to the $(r,\phi)$ and $\theta$ phase difference data using the interpolated E3 southern phase, as in *Provan et al.* [2013].
[g]Southern period estimated from linear interpolation of the southern phase between the end of interval E2 and the beginning of E4, as in *Provan et al.* [2013].

differences are collected for each interval in Table 1. Uncertainty ranges, also given in Table 1, are determined from the estimated uncertainties in the slope of the linear fit to the relative phase values (equations (3a) and (3b)) [*Andrews et al.*, 2012; *Provan et al.*, 2013].

The changes in phase banding in Figures 3d and 3e also indicate marked variations in the relative amplitudes of the southern and northern oscillations as shown in Figure 3g, with unexpected resumption of southern dominance in E2 ($k = 0.32$), reversing for the first time to northern dominance ($k \approx 6$) in E3, continued northern dominance in E4 though of lesser extent ($k = 1.56$) and then a modest southern preference again in F1 and F2 ($k = 0.96$ and 0.74, respectively). These $k$ values (with estimated uncertainties) are also collected in Table 1. It should be noted that during E3 the modulation of the southern format data is sufficiently weak that a direct linear fit to these data is not possible (implying $k \geq 5$ as above). Given that only small jumps in phase are evident at the other boundaries, *Provan et al.* [2013] derived a tentative interpolated southern phase during this interval drawn as a dotted line between the end of E2 and the beginning of E4 in Figure 3d, the modulo 360° nature of these phase values being resolved by choosing the line that gives the most similar period to those in the adjacent intervals. The corresponding southern period is shown as a dotted red line in Figure 3f, yielding a value only slightly different to that during E4. Using this phase, an approximate fit to the $(r, \varphi)$ and $\theta$ phase deviations is then obtained with $k \approx 6$, as indicated above, shown as a dotted line in Figure 3g. In section 3.2 we examine the SKR data for evidence of such a period in the southern emissions.

The core region field component amplitudes are shown for the southern (solid and dotted lines) and northern (dashed lines) systems in Figure 3h, together with the Rev-by-Rev amplitude data from which they were derived, that vary at the beat period between values representing the sum and difference of the northern and southern amplitudes. The lines and data are color coded as for the phase data in Figures 3d and 3e. No results are shown for D2 since core region data are not available for this interval, and we recall that for F1 and F2, only $\varphi$-component values (blue) are available from short segments of unfiltered core data as the spacecraft passed north-south across the equatorial plane. The values derived from such data may not, therefore, be directly comparable with those determined from extended filtered residual data segments on near-equatorial orbits such as those occurring during E1–E4 [see, e.g., *Andrews et al.*, 2012]. Compared with the near-equal amplitudes for interval E1, southern amplitudes are seen to be enhanced and northern amplitudes reduced in E2, and vice versa in E3, while in the initial part of interval E4, all oscillations are found to be suppressed for the first time in the Cassini data set. Strong northern and somewhat weaker southern system oscillations then eventually emerge on a modeled time constant of ~70–110 days [*Provan et al.*, 2013]. For intervals F1 and F2, despite the above caveat, the $\varphi$-component amplitudes are seen to be reasonably compatible with those for E1 under similar $k \sim 1$ conditions. The physical origin of these significant amplitude variations remains unclear at present.

### 3.2. Comparison of Postequinox Magnetic and SKR Oscillation Properties

Given the altered nature of the magnetic oscillations observed since early 2011, both in amplitude and period, we now examine the extent to which this is reflected in SKR modulation properties. Although initial examination of the joint data set reveals the presence of small-scale features in the SKR modulation data that appear to be related to similar features in the magnetic oscillation data, such as the phase variations about the fitted linear southern phase in interval E2 (Figure 3d), here we concentrate on the significant longer time scale features associated with the intervals already identified and assign investigation of such short-term variations to future study.

As in the study by *Lamy* [2011], southern and northern emissions are identified on the basis of both their sense of circular polarization and their domain of visibility. As noted in section 1, southern and northern SKR extraordinary mode emissions are primarily left-hand (LH) and right-hand (RH) polarized, respectively, with the sources in one hemisphere illuminating the region down to ~20° latitude in the other [*Kaiser et al*., 1984; *Lamy et al*., 2008a, 2008b; *Kimura et al*., 2013]. LH emissions at latitudes less than +20° are thus taken to correspond to the Southern Hemisphere, while RH emissions at latitudes greater than −20° are taken to correspond to the northern. Emissions from both hemispheres can thus be monitored near continuously on near-equatorial orbits. Polarization-separated SKR powers, normalized to a fixed Saturn distance, are determined by integrating the emission spectra over the frequency band 40–500 kHz, thus excluding lower frequency narrowband emissions. Normalized periodograms are then formed from this generally temporally discontinuous data set by Lomb-Scargle analysis of the logarithm of the northern and southern integrated powers. The latter analysis uses a 200 day data window computed with a 1 day resolution.

Figures 4a and 4d show gray-scaled southern (LH) and northern (RH) SKR periodograms respectively, plotted with the modulation period (hours) on the vertical axis versus time, over the same interval as Figure 3, $t = 1827 - 3510$ days (1 January 2009 to 10 August 2013 inclusive). Year boundaries, Rev markers, and interval identifiers are again shown at the top of both plots, with vernal equinox being shown by the vertical dotted line and interval boundaries by the vertical dashed lines, as in Figure 3. The plots thus overlap with those shown previously by *Lamy* [2011] spanning January 2004 to mid-October 2010 within E1 (as in Figure 2), but here newly extend to later intervals where the magnetic oscillation data indicate closely spaced southern and northern periods with abrupt amplitude and phase transitions as discussed in section 3.1. A number of prominent peaks are observed in these periodograms that we compare with the magnetic oscillation periods.

Figures 4b and 4e show the same periodograms, but now with the magnetic oscillation periods for the southern system (red line) and northern system (blue line) from Figure 3f superposed on both. In Figure 4b it can be seen that the southern magnetic period follows the principal continuous peak in the southern periodogram throughout E1 as expected, though with a slightly longer period than that derived directly from the periodogram by *Lamy* [2011] during the first part of the interval, as discussed in section 2, leading to the relative shift in phase of ~180° shown in Figure 2f. The periods determined by *Lamy* [2011] to mid-2010 are shown for reference in Figures 4c and 4f, for the southern (red line) and northern (blue line) emissions, respectively. For the northern periodogram, however, it can be seen in Figures 4e and 4f that while both magnetic and SKR periods follow the prominent peak in the northern periodogram during interval D2, they diverge thereafter in interval E1. The SKR period follows a continuous but weaker peak that coalesces with the strong peak at the southern period near $t \approx 2290$ days (early April 2010) and remains so for more than ~100 days thereafter. The magnetic period in E1, however, does not initially correspond to any peak in the SKR periodogram, giving rise to the large deviations in relative phase shown in Figure 2f. However, after $t \approx 2500$ days (early November 2010) toward the end of E1, beyond the interval analyzed by *Lamy* [2011], it is evident that the most prominent peak in the northern periodogram returns to lower periods, below that of the southern period, that is seen in Figure 4e to be in good accord with the northern period determined from the magnetic data.

One complicating factor in considering these SKR periodograms is that, particularly during the intervals of near-continuous equatorial coverage, periodicities may appear in one hemisphere that are associated with the period of the other, as noted previously by *Lamy* [2011] for the preequinox data interval. For example, peaks at the southern period are clearly present in the northern periodogram throughout much of E1, and vice versa during the later part of the interval. In these circumstances, the assignment of a particular period to a particular hemisphere may not be without some ambiguity on occasion, though this can be resolved by comparison with the magnetic oscillation periods. The physical mechanism responsible for this

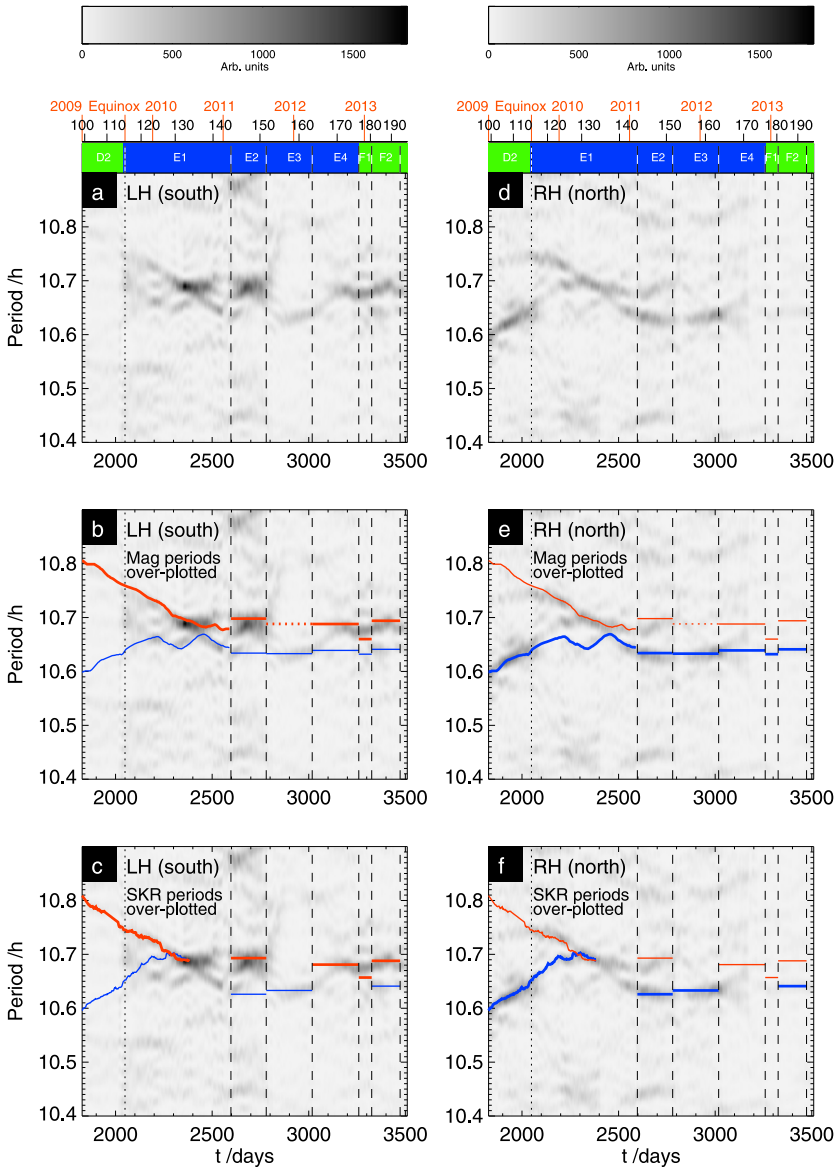


**Figure 4.** (a) Gray-scaled Lomb-Scargle periodograms of the PPO modulations of the LH polarized (south) SKR emissions, with modulation period (hours) plotted versus time in the range $t = 1827 - 3510$ days (1 January 2009 to 10 August 2013 inclusive), as in Figure 3. The periodograms are computed using 200 day SKR data windows with 1 day resolution. Year boundaries, Rev numbers, and interval identifiers are shown at the top of the plot in the same format as Figures 2 and 3, with a vertical dotted line showing the time of vernal equinox and vertical dashed lines showing the times of the sharp magnetic oscillation amplitude and phase transitions that define intervals E1–E4 and F1 and F2. (b and c) The same periodogram, but now with the southern (red line) and northern (blue line) magnetic oscillation periods overplotted in Figure 4b, and with the SKR periods determined from the principal peaks in the southern and northern periodograms being similarly overplotted in Figure 4c. The magnetic periods are those shown in Figure 3f. The SKR periods shown in intervals D2 and the initial part of E1 are from *Lamy* [2011], while those shown for intervals E2 to F2 were determined using SKR data segments limited to these individual intervals, as shown in Figure 5. Figures 4d–4f show results in the same format as Figures 4a–4c but now for the gray-scaled Lomb-Scargle periodograms for the RH polarized (north) SKR emissions.

effect is not yet established, interhemispheric current flow in the PPO current system being one possibility [e.g., *Southwood and Kivelson*, 2007; *Southwood and Cowley*, 2014].

We now turn to the later interval characterized by sharp changes in the magnetic oscillation amplitudes and periods, occurring at the times indicated by the vertical dashed lines in Figure 4 marking intervals E2 to F2. The constant oscillation periods in these intervals obtained from piecewise linear fits to the magnetic phase

data shown in Figures 3d–3f are again overplotted on the southern and northern periodograms in Figures 4b and 4e. Starting with interval E2, it can be seen that separate prominent peaks are present in both southern and northern SKR periodograms that are essentially coincident with the southern and northern periods determined from the magnetic data. This result, together with the SKR data for the later interval of E1, confirms that as for the magnetic periods, the SKR periods near coalesced during interval E1 and then separated again in the late 2010 with the southern period remaining somewhat larger than the northern.

Noting again that the SKR periodograms are formed from 200 day running segments of radio data that will smooth sharp features on the ~100–200 day time scales of the magnetic oscillation transitions, to take the comparison of periods further we have adopted the magnetic intervals and have computed SKR periodograms for these specific segments of data. These are shown in Figure 5, where we plot the spectral power (arbitrary units) versus period from the Lomb Scargle analysis for each of the intervals E2 to F2. Those for E2 are shown in Figures 5a and 5b for the southern (LH) and northern (RH) emissions, respectively. The red and blue arrows with error bars at the top of these plots and corresponding red and blue vertical dotted lines show the magnetic periods for the southern and northern systems, respectively, corresponding to $10.698 \pm 0.003$ h for the southern system and $10.634 \pm 0.005$ h for the northern (Table 1). The peaks in the SKR periodograms marked by the black dotted vertical lines are at periods $10.693 \pm 0.019$ h and $10.626 \pm 0.014$ h, in excellent agreement with the magnetic periods within uncertainties, as can be seen in the figure. As noted in section 3.1, the uncertainties in the magnetic oscillation periods are determined from the uncertainties in the gradient of the linear fit to the magnetic phase data. As an initial estimate, the rather larger quoted uncertainties in the SKR periods are instead given by the full width at half maximum (FWHM) of the corresponding spectral peak, conditioned by the length of the data interval employed, though empirical evidence discussed below suggests that these values have the nature of upper limits. These SKR periods and uncertainties are also collected in Table 1. It can be seen in Figure 5b that a secondary peak is present in the northern periodogram at the southern period during E2, but not vice versa in Figure 5a. The SKR periods are also shown by the horizontal red and blue lines in Figures 4c and 4f, where they are seen to agree closely with the running 200 day periodogram peaks as expected.

Recalling that interval E2 saw the reemergence of southern magnetic oscillation dominance following near-equal amplitudes in E1, it is also of interest to examine whether the SKR spectral powers show any corresponding features. It can be seen in Figures 4a and 4b that the southern spectral power near the southern period increased significantly in E2 compared with the end of E1, in possible correspondence with the increase in the southern magnetic amplitude by a factor of ~2 across this boundary (Figure 3h). The northern spectral power near the northern period in Figures 4d and 4e is also seen to reach a local maximum near this boundary before decreasing again by the middle of E2, possibly reflecting the more than factor ~2 drop in the northern magnetic amplitude.

For interval E3 we recall from section 3.1 that the magnetic data show a sharp switch from southern dominance in E2 to northern dominance in E3, involving a factor of ~3 increase in the northern amplitude to values comparable with or larger than those in E1, while the southern amplitude decreased by a factor of at least ~6, below that allowing direct detection of the southern period. Correspondingly, in Figures 4d and 4e a prominent peak is present in the northern emission periodogram during this interval, the spectral power of which grows significantly with time, and the period of which is closely comparable with the northern magnetic period. The peak in the northern periodogram shown for this interval in Figure 5d occurs at $10.633 \pm 0.010$ h, in excellent agreement with the magnetic period of $10.633 \pm 0.002$ h (Table 1).

Essentially the same period is also present in the southern SKR periodogram in Figures 4a and 5c, which could either represent an observation of the northern period in the southern data similar to that reported above for E2 and previously by *Lamy* [2011], or possibly it could represent a closely coalesced "true" southern period during the interval. This finding thus prompts brief consideration of whether a southern magnetic oscillation could be present with a period closely similar to the northern period during this interval. For such an oscillation with a significant amplitude of $k$ less than ~5, say, to remain undetected in the magnetic phase data (showing closely northern polarization throughout in Figure 3), it can readily be shown that not only would the period have to remain within $\sim 10^{-3}$ h of the northern period throughout (compared with differences of $\sim 5 \times 10^{-2}$ h in adjacent intervals) but also that the relative phase would have to lie

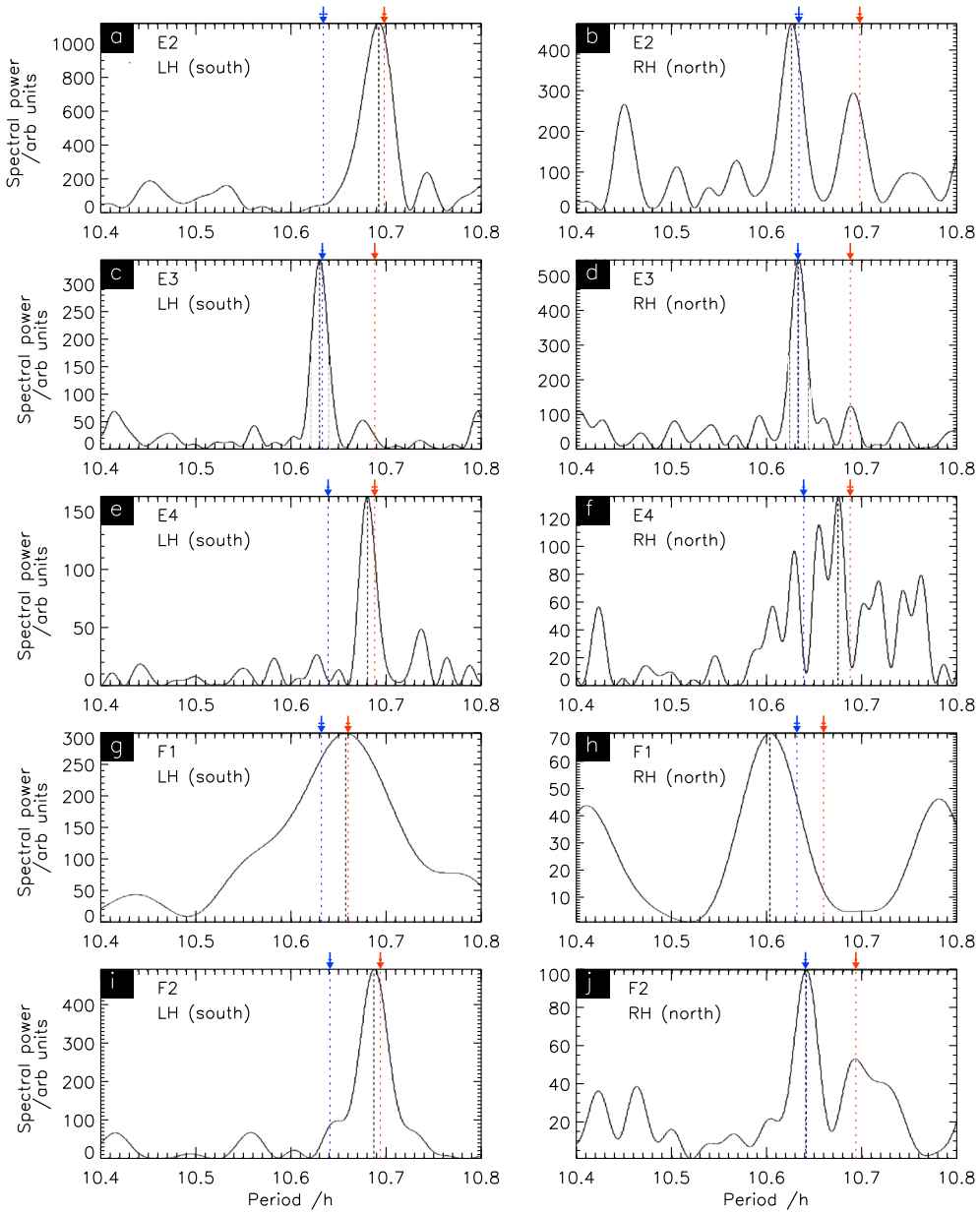


**Figure 5.** Lomb-Scargle periodograms of SKR power modulations determined over intervals E1 to F2 defined by the magnetic oscillation data. Each plot has been scaled to the maximum value of the spectral power, marked by the black vertical dotted lines. (a, c, e, g, and i) Periodograms derived from LH polarized (south) power data for each interval as marked. (b, d, f, h, and j) Periodograms derived from RH polarized (north) power data for the same intervals. The arrows at the top of each plot show the southern (red) and northern (blue) periods determined from the magnetic oscillation data, continued into the plot panel by similarly colored vertical dotted lines. The horizontal bar on each arrow shows the estimated uncertainty interval when wider than the arrow (except for the southern magnetic period in E3 (Figures 5c and 5d), obtained by interpolation of the oscillation phase between E2 and E4).

within a few degrees of either in-phase or antiphase with the northern oscillation. However, this implausibly fine-tuned scenario would also yield unusual values of the field component amplitude ratios, with $r$ and $\phi$ amplitudes enhanced and $\theta$ reduced for in-phase oscillations, and vice versa for antiphase, for which there is no evidence in the amplitude data. Instead, the amplitude ratios during E3 indicated in Figure 3h are entirely typical of other intervals [e.g., *Provan et al.*, 2013], yielding a lower limit on the value of $k$ of ~10–20, greater than the limiting relative amplitude for a general southern oscillation of any period.

It thus seems far more plausible to suggest that the LH (south) SKR peak in E3 in Figures 4a and 5c represents observation of the northern period in the Southern Hemisphere data, similar to the reverse situation in E2 when the southern system was dominant. However, there is no evidence in the southern SKR data for a significant secondary peak at another value that might represent the southern period, in particular, none at the estimated southern magnetic period determined from interpolation of the southern phase (red arrow and dotted line in Figures 5c and 5d), thus reinforcing its tentative nature indicated in section 3.1 above. Both SKR and magnetic field data are thus consistent with a reduction in the southern oscillation amplitude to below detectability during this ~240 day interval.

We now consider interval E4, together with its continuation into F1 and F2. We recall that the magnetic data indicate the suppression of all regular PPO activity at the start of E4, the amplitude then growing over ~100 days to strong oscillations by its end with $k \approx 1.6$, such that the northern oscillations were stronger than the southern but not by a large factor (Figures 3g and 3h). Correspondingly, the southern SKR periodogram in Figure 4a shows the growth of a single significant peak during E4, which the comparison with the magnetic periods in Figure 4b shows lies close to the southern magnetic period. The SKR period determined from the E4 data alone (Figure 5e) is $10.681 \pm 0.010$ h shown by the red line in Figure 4c, while the southern magnetic period is $10.688 \pm 0.004$ h, thus in agreement within the uncertainty estimates. This southern SKR peak continues at similar periods in Figure 4a into intervals F1 and F2 and does not clearly exhibit the short-lived sharp drop in southern magnetic period observed in F1 as shown in Figure 4b. This is not surprising given the 200 day window of the SKR determination and the ~70 day interval of F1. However, selecting SKR data just for interval F1 then yields a period of $10.657 \pm 0.062$ h, closely similar to the southern magnetic period of $10.660 \pm 0.003$ h, though as shown in Figure 5g the periodogram peak is very broad, as indicated by the uncertainty estimate. In F2 the southern SKR period then returns to values similar to E4, $10.688 \pm 0.017$ h as shown in Figures 4c and 5i, again closely similar to the southern magnetic period of $10.694 \pm 0.001$ h.

Turning now to the northern periodograms shown in Figure 4d, it can be see that, as for the southern periodograms, no single continuous peak is present near the start of interval E4. However, a weak continuous peak emerges toward the middle of E4 with a similar period to that in E2 and E3, and continues into F1 and F2, that approximately coincides with the northern magnetic period shown in Figure 4e. However, this peak is too weak and ill defined in E4 and F1 to derive reliable northern SKR periods (Figures 5f and 5h). In F2, while remaining weak it becomes somewhat more clearly defined (Figure 5j), yielding a period of $10.641 \pm 0.015$ h equal to the northern magnetic period of $10.641 \pm 0.002$ h in the same interval (Table 1). The weakness of the northern signal relative to that in the southern periodograms may initially seem surprising given the fact that the northern magnetic oscillation amplitude is greater than (E4) or comparable with (F1 and F2) that of the southern oscillation during this interval (Figures 3g and 3h). However, Figure 3b shows that the spacecraft orbit became increasingly inclined during E4, and into F1 and F2, with apoapsis in the Southern Hemisphere, thus favoring observation of the southern SKR sources.

The emergence of inclined orbits during intervals E4–F2 does, however, allow us to divide the SKR data by a different method which unequivocally establishes the hemisphere of emission. Rather than divide the data principally by the circular polarization of the emission, we instead select a southern data set for these later intervals that only contains data from southern spacecraft latitudes and a northern data set that only contains data from northern spacecraft latitudes, thus excluding data from the equatorial region. We recall that the polarization-separated data employed in Figure 4 included all data from latitudes less than +20° for LH (south) emissions, and from latitudes greater than −20° for RH (north) emissions, thus including all the near-equatorial data. As noted in section 3.2, the latitude limits here arise from the fact that the sources in one hemisphere can illuminate the region down to ~20° latitude in the other [*Lamy et al.*, 2008a]. However, in the interests of preserving more data in the analysis, here we have employed a slightly less severe latitudinal restriction, forming a "Northern Hemisphere" data set from all data obtained above +10° latitude, and a "Southern Hemisphere" (SH) data set from all data obtained below −10° latitude. We note that *Gurnett et al.* [2009a] have shown that such a ±10° limit generally provides sufficient hemispheric discrimination [see also *Kimura et al.*, 2013, Figure 4]. We also confine attention to the stronger signals in the southern data for reasons indicated above and in Figure 6 compare the gray-scaled periodograms derived for intervals E4 to F2 from the polarization-separated LH (south) data shown in Figure 6a (as in Figure 4a), with that for the latitudinally separated SH data shown in Figure 6c. These periodograms are repeated in Figures 6b and 6d, respectively, where we now overplot the southern magnetic oscillation period on both (red line). Although the SH periodogram is somewhat noisier than the LH

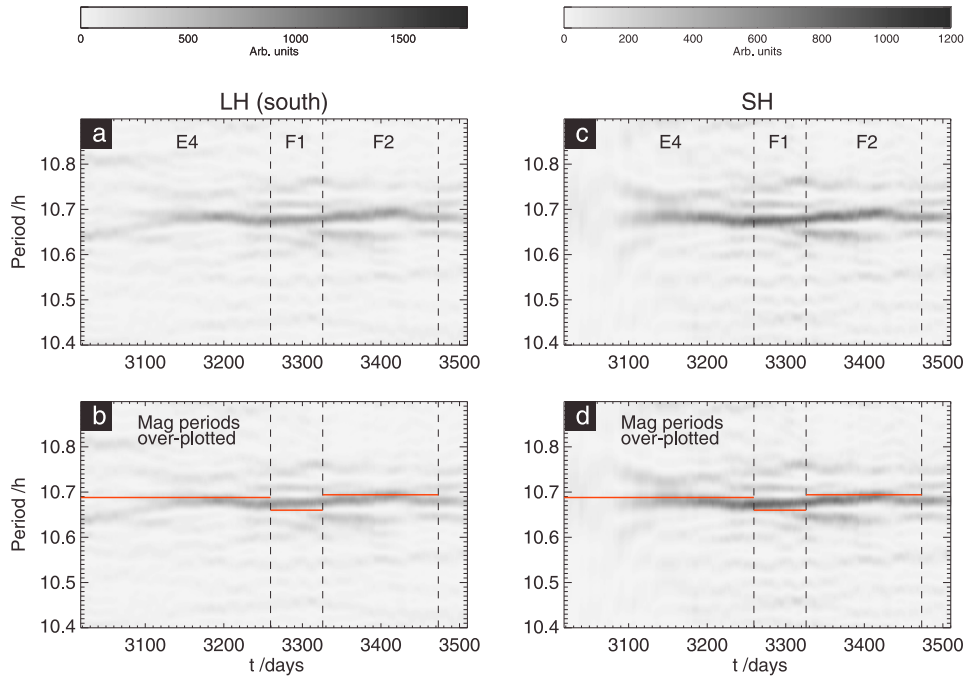


**Figure 6.** Plots comparing the southern SKR periodograms obtained using two methods of hemispheric separation, with and without use of the state of circular polarization of the emission, applied to the interval of inclined orbits during E4 to F2 (vertical dashed lines, see Figure 3b). (a) Selects SKR powers with LH (south) polarization as in Figure 4a and employs all data for spacecraft latitudes less than +20°, thus, in particular, employing all near-equatorial data. (c) Does not employ polarization-separated SKR power data but instead employs all data observed at spacecraft latitudes less than −10°, forming a Southern Hemisphere (SH) periodogram. (b and d) Repeat the periodograms in Figures 6a and 6c, respectively, but now have the southern period determined from the magnetic oscillation data overplotted (red lines).

(south) periodogram since it is perforce based on less data, it can be seen that the two periodograms are essentially identical in form, with a continuous principal peak that agrees closely with the southern magnetic period within the limit imposed by the use of 200 day segments of SKR data. These results thus confirm that the corresponding SKR modulation is associated with Southern Hemisphere emissions.

### 3.3. Relative Phases of Postequinox Magnetic Oscillations and SKR Modulations

We now wish to determine the relative phases of the magnetic oscillations and SKR modulations in the later postequinox interval newly examined here, in order to compare results with the preequinox and equinoctial determinations shown in Figure 2f and discussed in section 2. Given the variable nature of the postequinox SKR data evident in Figure 4, it is not straightforward to develop overall models of the southern and northern SKR phases. Nevertheless, it is straightforward to derive piecewise linear models of the SKR modulation phase for the postequinox intervals identified above in which a prominent spectral peak is present (Figure 5 and Table 1) and to compare these with the similarly piecewise linear oscillation phases derived from the magnetic data in the same intervals (as in Figures 3d and 3e).

An issue with regard to such comparisons exists, however, on consideration of the formal uncertainties in the period values quoted above and in Table 1. While the uncertainties in the magnetic oscillation periods, on average ~0.002 h, yield only modest uncertainties in phase of ~±15° over typical intervals of ~150–200 days (meaning deviations in phase varying from ~+15° at one end of the interval to ~−15° at the other), those associated with the SKR periods, on average ~0.021 h, are instead ~±140°, which would render any comparison of the phases meaningless. Even if we exclude from consideration the SKR value for short interval F1 having a very large formal uncertainty, the average uncertainty in SKR period is only reduced to ~0.014 h, 6 times the magnetic field value, yielding a phase uncertainty of ~±95° over such intervals. Examination of the relative magnetic field and SKR periods in Table 1, however, derived from independent analyses of different data sets, shows that all of the magnetic periods are either equal to the SKR values or slightly longer, with an averaged

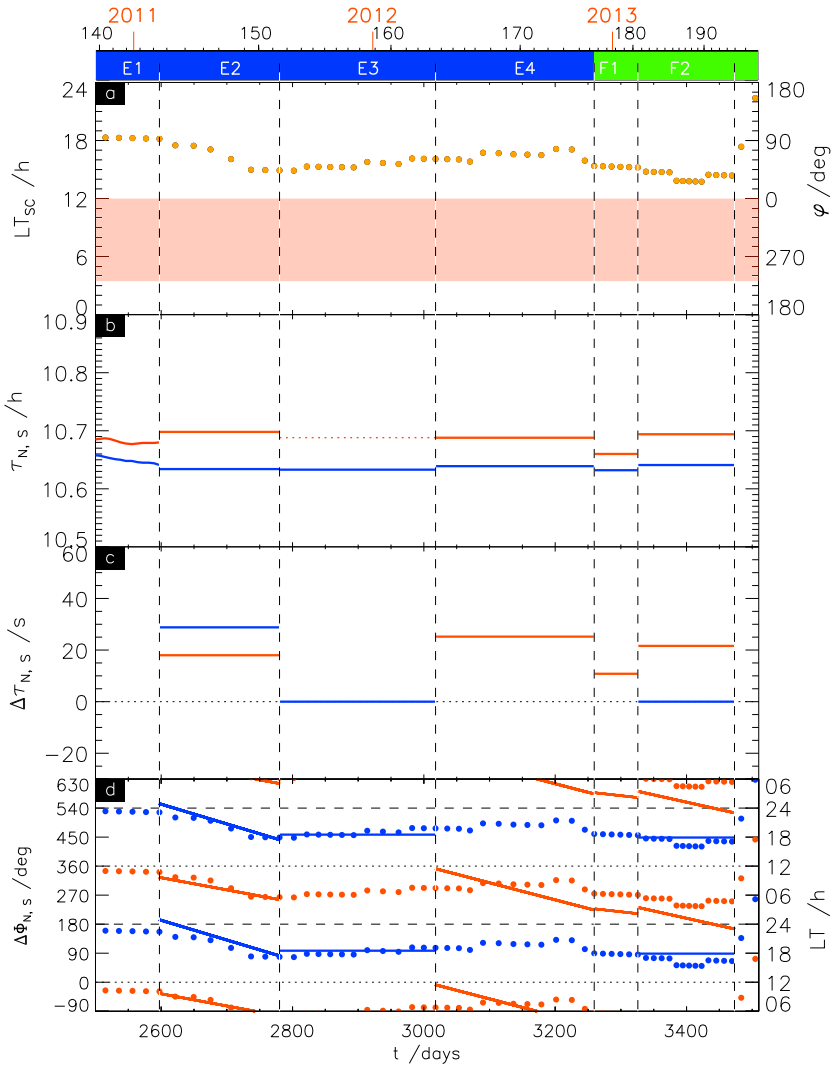


**Figure 7.** Plot showing Cassini orbital parameters and PPO data spanning intervals E2–F2, specifically for $t = 2500 - 3510$ days, in a format related to Figure 2. Vertical dashed lines mark the boundaries of the intervals as in Figures 3 and 4. (a) The LT of spacecraft apoapsis on each Rev as in Figure 3c (orange dots), plotted at the time of apoapsis, with an equivalent azimuth scale being shown on the right. The red band indicates the LT range in which SKR strobe modulations will be observed at the spacecraft, between ~3.5 and ~12 h LT as indicated by equation (4b), caused by the dominant postdawn SKR sources. (b) The magnetic oscillation periods (hours) for the southern (red) and northern (blue) systems, as in Figure 3f. (c) The difference in magnetic and SKR oscillation periods (seconds) $\Delta\tau_{N,S} = \tau_{Mag\ N,S} - \tau_{SKR\ N,S}$ for the southern (red) and northern (blue) systems, when both are determined (Table 1). (d) The solid lines show the piecewise magnetic-SKR difference phases for the southern (red) and northern (blue) systems, defined as $\Delta\Phi_{N,S} = \Phi_{Mag\ N,S} - \Phi_{SKR\ N,S}$ (as in Figure 2f), which gives the azimuth of the equatorial quasi-uniform field for each system at times of corresponding SKR maxima (when $\Phi_{SKR\ N,S} = 360\ N$ deg for integer $N$). The slopes of these lines reflect the small differences in period shown in Figure 7c. The red and blue dots in Figure 7d plotted at the times of spacecraft apoapsis show the simple model difference phases for the southern and northern systems, respectively, based on equations (4a), (4b), (5a) and (5b), assuming that the azimuth of spacecraft apoapsis is a reasonable representative value of the overall spacecraft azimuth on each orbit. Two cycles of phase are shown on the vertical axis, with an equivalent LT scale to the right. The model source azimuth itself is 90° ahead of the red dots, or equivalently 90° behind the blue dots (equations (5a) and (5b)).

difference in period of only 0.004 h. This value is a factor of ~1.7 larger than the averaged uncertainty in the magnetic field periods, but a factor ~3.4 less than the smaller of the above estimated uncertainties in the SKR periods (a factor of ~5.1 less for the overall average). Assuming uncorrelated errors, this suggests that the overall uncertainties in the SKR periods are instead ~ ±0.003 h, similar to but a little larger than the magnetic field errors, and significantly less than the formal errors by a factor of ~4. In this case, the uncertainties in SKR phase

over the above intervals are reduced to ~ ±20°, with a combined uncertainty in the difference between the two phases of ~ ±25°. We thus suggest that the magnetic and SKR phase differences determined here are likely meaningful within an uncertainty of this order, rather than a value ~5 times larger.

Results are shown in Figure 7 for intervals E2–F2, specifically encompassing $t = 2500 - 3510$ days, in a format related to Figure 2. Figure 7a first shows the LT of spacecraft apoapsis (orange dots), which, for near-equatorial observations, is indicative of the LT of the SKR emission sources to which the radio data is responding, as discussed further below. Figure 7b then shows the magnetic oscillation periods for the southern (red) and northern (blue) systems as in Figure 3f, while Figure 7c similarly shows the difference between the magnetic and SKR periods for the two systems $\Delta\tau_{N,S} = \tau_{Mag\ N,S} - \tau_{SKR\ N,S}$, when both are determined (Table 1), all being zero within a resolution of ~2 s (0.0005 h) or small positive values ~20 s as indicated above. The solid lines in Figure 7d then show the piecewise difference phases for the southern (red) and northern (blue) systems, defined as in section 2 and Figure 2f as $\Delta\Phi_{N,S} = \Phi_{Mag\ N,S} - \Phi_{SKR\ N,S}$, which gives the azimuth of the equatorial quasi-uniform field for each system at times of corresponding SKR maxima (occurring when $\Phi_{SKR\ N,S} = 360\ \ N$ deg for integer $N$). The slopes of these lines reflect the small differences in magnetic and SKR periods shown in Figure 7c.

At the start of the interval the spacecraft apoapsis was located near the dusk meridian as shown in Figure 7a, as had been the case previously throughout interval E1. The difference phase for the southern system in Figure 7d shows that in interval E2 the southern quasi-uniform field pointed toward the prenoon to dawn sector at southern SKR maxima, comparable with the situation in the central interval of E1 shown in Figure 2f. As indicated in sections 1 and 2, since the upward field-aligned current associated with the southern system is expected to peak ~90° of azimuth ahead of the related quasi-uniform field, this configuration implies that the observed southern SKR modulation in E2 was then caused by sources in the noon to postnoon sector rather than those in the postdawn sector under earlier preequinox orbital conditions. Correspondingly, the difference phase for the northern system in E2 indicates that the northern quasi-uniform field pointed ~180° away from this direction in the midnight to dusk sector at northern SKR maxima, for the first time also consistent with a response to sources in the postnoon to dusk sector rather than to those in the postdawn sector earlier in the mission. This follows from the expectation that the upward field-aligned current associated with the northern system should peak ~90° of azimuth behind the related quasi-uniform field.

Figure 7 shows, however, that spacecraft apoapsis moved from dusk toward noon within E2, then slowly back toward dusk in E3 and E4, before returning to the postnoon sector in F1 and F2. Overall, the difference phases also move to smaller values, though more so for the southern system than for the northern. In F2 the southern quasi-uniform field pointed toward the postmidnight to midnight sector at southern SKR maxima, as in the preequinox interval, indicative of a response to the principal SKR sources in the postdawn sector. The northern quasi-uniform field in F2 pointed toward dusk at northern SKR maxima, indicative of responses to sources in the noon sector.

A simple expression for the expected direction of the northern and southern quasi-uniform fields at corresponding SKR maxima can be derived using model results presented by *Andrews et al*. [2011]. Their model takes simple account of the SKR sources visible at near-equatorial observation points resulting from the hollow conical beaming pattern of the radiation, thus avoiding issues around the complex source visibility effects that occur at high latitudes, noting in Figure 3b that the spacecraft apoapsis remained at modest latitudes throughout the interval investigated here, including the later interval of inclined orbits. Under these circumstances, *Andrews et al*. [2011] showed that the effective azimuth of the SKR source $\varphi_{source}$ when the spacecraft is located at azimuth $\varphi_{sc}$ can be approximated as

$$\varphi_{source} = 296° + \left(\frac{180°}{116°}\right)\ \varphi_{sc}(\text{deg}) \qquad \text{for} \quad 0° \le \varphi_{sc}(\text{deg}) \le 232° \tag{4a}$$

and

$$\varphi_{source} = 296° \qquad \text{for} \quad 232° \le \varphi_{sc}(\text{deg}) \le 360°, \tag{4b}$$

representing a simplified summary of the numerical results shown by the solid line in their Figure 2c. The effective source azimuth thus corresponds to the principal postdawn sources centered at azimuth 296° (~7.7 h LT) for observations over the whole azimuthal region from 232° (~3.5 h LT) to 360° (12 h LT), giving rise to the "strobe" modulation effect in this broad LT sector (equation (4b)) as discussed in section 1. Outside this

region the effective source azimuth is then skewed away from the observer's azimuth toward these principal sources on either side of their antipodal azimuth at 116° (~19.7 h LT) (equation (4a)). On the expectation that maximum SKR power is emitted when the upward currents of the PPO current systems are superposed on the effective source, as indicated above and in sections 1 and 2, the difference phases are then given by

$$\Delta\Phi_N \approx \varphi_{\text{source}}(\varphi_{\text{sc}}) + 90° \tag{5a}$$

and

$$\Delta\Phi_S \approx \varphi_{\text{source}}(\varphi_{\text{sc}}) - 90°, \tag{5b}$$

where $\varphi_{\text{source}}(\varphi_{\text{sc}})$ is given by equations (4a) and (4b).

The red band in Figure 7a shows the LT region in which a spacecraft will observe the SKR strobe effect according to equation (4b), i.e., between ~3.5 h and 12 h LT as indicated above. The orange dots in this panel then show that apoapsis, where the spacecraft spends most of its time, is located well outside of this range in the early part of the interval, such that local duskside SKR sources will then be significant. However, apoapsis then moves toward this band during E2 and in F1 and F2, such that the more powerful postdawn sources will become increasingly influential. Assuming that the azimuth of apoapsis is a reasonable representative value of the overall spacecraft azimuth on each orbit, the red and blue dots in Figure 7d (plotted at the time of apoapsis as in Figure 7a) show the simple model values of the difference phases for the southern and northern systems, respectively, based on equations (4a), (4b), (5a), and (5b). (The model source azimuth itself is 90° (6 h LT) ahead of the southern system red dots, or equivalently 90° behind the northern system blue dots, as indicated by equations (5b) and (5a).) It can be seen that there is reasonable consistency between the observed difference phases and the simple model for both southern and northern systems, indicating that the overall drift in difference phase over the interval toward smaller values more nearly similar to those observed earlier in the mission, is likely due to the shift in orbit apoapsis from dusk back toward noon. The level of this consistency also appears compatible with the reduced uncertainties in the phase difference discussed above, rather than anything very much larger. The overall positive values of the difference periods in Figure 7c are also likely influenced by this effect. The rotation of spacecraft apoapsis through an azimuth of ~70° to earlier LTs over the whole interval, producing a reduction in the effective azimuth of the SKR sources by ~105° according to equation (4a), will result in an apparent reduction of the SKR period relative to the magnetic field period of ~6 s over the whole interval, compared with an overall averaged value in Figure 7c of ~14 s.

## 4. Summary and Conclusions

In this paper we have newly compared the Saturn PPO properties determined from Cassini magnetic field data in the postequinox interval with the related modulations observed in the SKR emission data. This comparison is of particular significance due to the unanticipated behavior of the oscillation properties during this interval to date, involving closely spaced southern and northern periods centered near ~10.67 h, the southern period being slightly longer than the northern by ~3 min (Table 1), with sharp simultaneous changes in the southern and northern oscillation amplitudes, periods, and sometimes phases at ~100–200 day intervals. Six such transitions have been observed to date, between early 2011 and mid-2013 (Table 1). Our results show that when periods can reliably be determined from the SKR data during this interval, which, as for the magnetic field data, is not invariably the case, the values determined from the SKR data are in excellent agreement with those derived from the magnetic field data. Thus, during interval E2, for example, spanning early February to early August 2011, both data sets indicate a southern period near 10.69 h and a northern period near 10.63 h. Such basic correspondence is expected, of course, since both oscillatory phenomena are believed due to the same underlying rotating current systems, southern and northern. However, demonstrating this fact is significant in confirming that the southern period remained slightly longer than the northern during this postequinox interval, despite the near coalescence in periods at some point during 2010, whose timing is judged to be somewhat earlier in the SKR data (centered in late June) than in the magnetic field data (centered in late September).

Interpretation of the SKR results is complicated by the presence, particularly in near-equatorial polarization-separated data, of modulation in the emission from one hemisphere that appears to be associated principally with the other. This phenomenon was previously reported in earlier southern summer SKR data by *Lamy*

[2011], possibly associated with interhemispheric field-aligned current flow in the PPO current system and is also clearly present in the data here. In the data set analyzed in interval E3, for example, between early August 2011 and early April 2012 when the northern oscillations were overwhelmingly dominant in the magnetic data, the only significant peak occurring in the LH (south) periodograms were those associated with the northern period. The magnetic data show that the southern oscillations had essentially disappeared during this interval, with none in particular being measureable at the northern period, which strongly indicates that only the northern period was being observed in the SKR data, both north and south.

During subsequent intervals E4 to F2, to the end of the joint data set in early July 2013, stronger modulations were observed in the southern (LH) compared with the northern (RH) SKR data, due possibly to the tilt of Cassini apoapsis into the southern hemisphere ($\lambda \approx -35°$) favoring observation of southern sources. Where the modulation periods could be determined, these were again found to be in excellent accord with those derived from the magnetic field data. Confirmation of the hemisphere of origin of the stronger southern SKR modulations has been obtained during this later interval by undertaking an analysis of SKR data separated only by latitude, rather than principally by polarization, as employed during the earlier intervals of near-equatorial orbits (E1–E3).

It has also been found that the SKR data show some effects that appear to be related to the sharp simultaneous changes in the southern and northern oscillation amplitudes observed in the magnetic field data during this interval, such as the sharp resumption of southern dominance in E2 from near-equal amplitudes in E1, then reversing to northern dominance in E3. Correspondingly, the SKR data show an increase in the spectral power at the southern period in E2 and a cessation in E3, while the spectral power at the northern period declines during E2 and increases again during E3. However, the correspondence is by no means exact, due first to the running 200 day data intervals used to derive the gray-scaled periodograms and second to likely "seeing" effects associated with the conically beamed SKR emissions. Thus, for example, during intervals E4 to F2 when the spacecraft apoapsis became tilted into the Southern Hemisphere, the southern SKR modulations are significantly more pronounced than the northern, as indicated above, despite the magnetic data showing modest northern dominance ($k \approx 1.6$) during E4 and similar amplitudes during F1 and F2 ($k \approx 0.96$ and 0.74, respectively).

Examination of the phase difference between the magnetic and SKR oscillations in the postequinox interval shows that during E2 when spacecraft apoapsis was located in the dusk to predusk sector, the southern quasi-uniform field pointed to the prenoon to dawn sector at southern SKR maxima, while the northern quasi-uniform field pointed ~180° away to the midnight to dusk sector at northern SKR maxima. Both are indicative of a response to SKR sources centered more locally to the spacecraft in the postnoon to predusk sector, rather than to the more powerful sources in the postdawn sector that dominated preequinox observations. By intervals F1 and F2, however, the spacecraft apoapsis had rotated into the postnoon sector, where the southern quasi-uniform field pointed toward the postmidnight to midnight sector at southern SKR maxima, while the northern quasi-uniform field pointed toward dusk, both indicative of responses to sources in the noon to dawn sector, more similar to those observed in earlier preequinox interval [*Andrews et al*., 2008; *Provan et al*., 2011].

Overall, the combined magnetic and SKR results thus confirm that following near coalescence of the southern and northern PPO periods for an interval during mid-2010, no enduring reversal in the two periods took place to mid-2013, this 4 years after vernal equinox and nearly halfway to northern solstice in May 2017. The planetocentric latitude of the Sun at Saturn had reached ~19° at the end of the interval studied here (Figure 3), significantly more than halfway to its maximum solstice value of ~27°. Although the long-term post-Voyager behavior after the last vernal equinox in 1980 remains unknown, the behavior observed by Cassini is clearly at variance with any interpretation of the postautumnal equinoctial behavior observed by Ulysses (Figure 1). Further monitoring and analysis of the behavior of this phenomenon is clearly warranted.

**Acknowledgments**
Work at the University of Leicester was supported by STFC grant ST/K001000/1. L.L. was supported by the CNES. We thank S. Kellock and the Cassini Mag team at Imperial College for access to processed magnetic field data. Calibrated magnetic field and radio data from the Cassini mission are available from the NASA Planetary Data System at the Jet Propulsion Laboratory (https://pds.jpl.nasa.gov/).

Michael Liemohn thanks the reviewers for their assistance in evaluating this paper.

## References

Andrews, D. J., E. J. Bunce, S. W. H. Cowley, M. K. Dougherty, G. Provan, and D. J. Southwood (2008), Planetary period oscillations in Saturn's magnetosphere: Phase relation of equatorial magnetic field oscillations and SKR modulation, *J. Geophys. Res.*, *113*, A09205, doi:10.1029/2007JA012937.

Andrews, D. J., S. W. H. Cowley, M. K. Dougherty, and G. Provan (2010a), Magnetic field oscillations near the planetary period in Saturn's equatorial magnetosphere: Variation of amplitude and phase with radial distance and local time, *J. Geophys. Res.*, *115*, A04212, doi:10.1029/2007JA014729.

Andrews, D. J., A. J. Coates, S. W. H. Cowley, M. K. Dougherty, L. Lamy, G. Provan, and P. Zarka (2010b), Magnetospheric period oscillations at Saturn: Comparison of equatorial and high-latitude magnetic field periods with north and south SKR periods, *J. Geophys. Res.*, *115*, A12252, doi:10.1029/2010JA015666.

Andrews, D. J., B. Cecconi, S. W. H. Cowley, M. K. Dougherty, L. Lamy, G. Provan, and P. Zarka (2011), Planetary period oscillations in Saturn's magnetosphere: Evidence in magnetic field phase data for rotational modulation of Saturn kilometric radiation emissions, *J. Geophys. Res.*, *116*, A09206, doi:10.1029/2011JA016636.

Andrews, D. J., S. W. H. Cowley, M. K. Dougherty, L. Lamy, G. Provan, and D. J. Southwood (2012), Planetary period oscillations in Saturn's magnetosphere: Evolution of magnetic oscillation properties from southern summer to post-equinox, *J. Geophys. Res.*, *117*, A04224, doi:10.1029/2011JA017444.

Arridge, C. S., et al. (2011), Periodic motion of Saturn's nightside plasma sheet, *J. Geophys. Res.*, *116*, A11205, doi:10.1029/2011JA016827.

Badman, S. V., et al. (2012), Rotational modulation and local time dependence of Saturn's infrared $H_3^+$ auroral intensity, *J. Geophys. Res.*, *117*, A09228, doi:10.1029/2011JA017990.

Burch, J. L., A. D. DeJong, J. Goldstein, and D. T. Young (2009), Periodicity in Saturn's magnetosphere: Plasma cam, *Geophys. Res. Lett.*, *36*, L14203, doi:10.1029/2009GL039043.

Burton, M. E., M. K. Dougherty, and C. T. Russell (2010), Saturn's internal planetary magnetic field, *Geophys. Res. Lett.*, *37*, L24105, doi:10.1029/2010GL045148.

Carbary, J. F., and S. M. Krimigis (1982), Charged particle periodicity in the Saturnian magnetosphere, *Geophys. Res. Lett.*, *9*, 1073–1076.

Carbary, J. F., D. G. Mitchell, S. M. Krimigis, and N. Krupp (2007), Electron periodicities in Saturn's outer magnetosphere, *J. Geophys. Res.*, *112*, A03206, doi:10.1029/2006JA012077.

Carbary, J. F., D. G. Mitchell, P. Brandt, C. Paranicas, and S. M. Krimigis (2008a), ENA periodicities at Saturn, *Geophys. Res. Lett.*, *35*, L07102, doi:10.1029/2008GL033230.

Carbary, J. F., D. G. Mitchell, P. Brandt, E. C. Roelof, and S. M. Krimigis (2008b), Periodic tilting of Saturn's plasma sheet, *Geophys. Res. Lett.*, *35*, L24101, doi:10.1029/2008GL036339.

Clarke, K. E., et al. (2006), Cassini observations of planetary-period oscillations of Saturn's magnetopause, *Geophys. Res. Lett.*, *33*, L23104, doi:10.1029/2006GL027821.

Clarke, K. E., D. J. Andrews, A. J. Coates, and S. W. H. Cowley (2010a), Magnetopause oscillations near the planetary period at Saturn: Occurrence, phase and amplitude, *J. Geophys. Res.*, *115*, A08209, doi:10.1029/2009JA014745.

Clarke, K. E., D. J. Andrews, A. J. Coates, S. W. H. Cowley, and A. Masters (2010b), Magnetospheric period oscillations of Saturn's bow shock, *J. Geophys. Res.*, *115*, A05202, doi:10.1029/2009JA015164.

Cowley, S. W. H., D. M. Wright, E. J. Bunce, A. C. Carter, M. K. Dougherty, G. Giampieri, J. D. Nichols, and T. R. Robinson (2006), Cassini observations of planetary-period magnetic field oscillations in Saturn's magnetosphere: Doppler shifts and phase motion, *Geophys. Res. Lett.*, *33*, L07104, doi:10.1029/2005GL025522.

Desch, M. D., and M. L. Kaiser (1981), Voyager measurement of the rotation period of Saturn's magnetic field, *Geophys. Res. Lett.*, *8*, 253–256.

Dougherty, M. K., et al. (2005), Cassini magnetometer observations during Saturn orbit insertion, *Science*, *307*, 1266–1270.

Espinosa, S. A., and M. K. Dougherty (2000), Periodic perturbations in Saturn's magnetic field, *Geophys. Res. Lett.*, *27*, 2785–2788.

Espinosa, S. A., D. J. Southwood, and M. K. Dougherty (2003a), Reanalysis of Saturn's magnetospheric field data view of spin-periodic perturbations, *J. Geophys. Res.*, *108*(A2), 1085, doi:10.1029/2001JA005083.

Espinosa, S. A., D. J. Southwood, and M. K. Dougherty (2003b), How can Saturn impose its rotation period in a non-corotating magnetosphere?, *J. Geophys. Res.*, *108*(A2), 1086, doi:10.1029/2001JA005084.

Galopeau, P. H. M., and A. Lecacheux (2000), Variations of Saturn's radio rotation period measured at kilometer wavelengths, *J. Geophys. Res.*, *105*, 13,089–13,101.

Gurnett, D. A., W. S. Kurth, and F. L. Scarf (1981), Plasma waves near Saturn: Initial results from Voyager 1, *Science*, *212*, 235–239.

Gurnett, D. A., et al. (2005), Radio and plasma wave observations at Saturn from Cassini's approach and first orbit, *Science*, *307*, 1255–1259.

Gurnett, D. A., A. M. Persoon, W. S. Kurth, J. B. Groene, T. F. Averkamp, M. K. Dougherty, and D. J. Southwood (2007), The variable rotation period of the inner region of Saturn's plasma disk, *Science*, *316*, 442–445, doi:10.1126/science.1138562.

Gurnett, D. A., A. Lecacheux, W. S. Kurth, A. M. Persoon, J. B. Groene, L. Lamy, P. Zarka, and J. F. Carbary (2009a), Discovery of a north-south asymmetry in Saturn's radio rotation period, *Geophys. Res. Lett.*, *36*, L16102, doi:10.1029/2009GL039621.

Gurnett, D. A., A. M. Persoon, J. B. Groene, A. J. Kopf, G. B. Hospodarsky, and W. S. Kurth (2009b), A north-south difference in the rotation rate of auroral hiss at Saturn: Comparison to Saturn's kilometric radio emission, *Geophys. Res. Lett.*, *36*, L21108, doi:10.1029/2009GL040774.

Gurnett, D. A., et al. (2010a), A plasmapause-like density boundary at high latitudes in Saturn's magnetosphere, *Geophys. Res. Lett.*, *37*, L16806, doi:10.1029/2010GL044466.

Gurnett, D. A., J. B. Groene, A. M. Persoon, J. D. Menietti, S.-Y. Ye, W. S. Kurth, R. J. MacDowell, and A. Lecacheux (2010b), The reversal of the rotational modulation rates of the north and south components of Saturn kilometric radiation near equinox, *Geophys. Res. Lett.*, *37*, L24101, doi:10.1029/2010GL045796.

Gurnett, D. A., J. B. Groene, T. F. Averkamp, W. S. Kurth, S.-Y. Ye, and G. Fischer (2011), The SLS4 longitude system based on a tracking filter analysis of the rotational modulation of Saturn kilometric radiation, in *Planetary Radio Emissions VII*, edited by H. O. Rucker et al., pp. 51–64, Austrian Acad. Sci. Press, Vienna, Austria.

Kaiser, M. L., M. D. Desch, J. W. Warwick, and J. B. Pierce (1980), Voyager detection of non-thermal radio emission from Saturn, *Science*, *209*, 1238–1240.

Kaiser, M. L., M. D. Desch, W. S. Kurth, A. Lecacheux, F. Genova, B. M. Pedersen, and D. R. Evans (1984), Saturn as a radio source, in *Saturn*, *Space Sci. Ser.*, edited by T. Gehrels and M. S. Matthews, pp. 378–415, Univ. of Arizona Press, Tucson, Ariz.

Kimura, T., et al. (2013), Long-term modulations of Saturn's auroral radio emissions by the solar wind and seasonal variations controlled by the solar ultraviolet flux, *J. Geophys. Res. Space Physics*, *118*, 7019–7035, doi:10.1002/2013JA018833.

Krupp, N., et al. (2005), The Saturnian plasma sheet as revealed by energetic particle measurements, *Geophys. Res. Lett.*, *32*, L20S03, doi:10.1029/2005GL022829.

Kurth, W. S., A. Lecacheux, T. F. Averkamp, J. B. Groene, and D. A. Gurnett (2007), A Saturnian longitude system based on a variable kilometric radiation period, *Geophys. Res. Lett.*, *34*, L02201, doi:10.1029/2006GL028336.

Kurth, W. S., T. F. Averkamp, D. A. Gurnett, J. B. Groene, and A. Lecacheux (2008), An update to a Saturnian longitude system based on kilometric radio emissions, *J. Geophys. Res.*, *113*, A05222, doi:10.1029/2007JA012861.

Lamy, L. (2011), Variability of southern and northern SKR periodicities, in *Planetary Radio Emissions VII*, edited by H. O. Rucker et al., pp. 39–50, Austrian Acad. Sci. Press, Vienna, Austria.

Lamy, L., P. Zarka, B. Cecconi, R. Prangé, W. S. Kurth, and D. A. Gurnett (2008a), Saturn kilometric radiation: Average and statistical properties, *J. Geophys. Res.*, *113*, A07201, doi:10.1029/2007JA012900.

Lamy, L., P. Zarka, B. Cecconi, S. Hesse, and R. Prangé (2008b), Modeling of Saturn kilometric radiation arcs and equatorial shadow zone, *J. Geophys. Res.*, *113*, A10213, doi:10.1029/2008JA013464.

Lamy, L., B. Cecconi, R. Prangé, P. Zarka, J. D. Nichols, and J. T. Clarke (2009), An auroral oval at the footprint of Saturn's kilometric radio sources, co-located with the UV aurorae, *J. Geophys. Res.*, *114*, A10212, doi:10.1029/2009JA014401.

Lamy, L., et al. (2010), Properties of Saturn kilometric radiation measured within its source region, *Geophys. Res. Lett.*, *37*, L12104, doi:10.1029/2010GL043415.

Lamy, L., B. Cecconi, P. Zarka, P. Canu, P. Schippers, W. S. Kurth, R. L. Mutel, D. A. Gurnett, D. Menietti, and P. Louarn (2011), Emission and propagation of Saturn kilometric radiation: Magnetoionic modes, beaming pattern, and polarization state, *J. Geophys. Res.*, *116*, A04212, doi:10.1029/2010JA016195.

Lamy, L., R. Prangé, W. Pryor, J. Gustin, S. V. Badman, H. Melin, T. Stallard, D. G. Mitchell, and P. C. Brandt (2013), Multispectral diagnosis of Saturn's aurorae throughout a planetary rotation, *J. Geophys. Res. Space Physics*, *118*, 4817–4843, doi:10.1002/jgra.50404.

Mardia, K. V., and P. E. Jupp (2000), *Directional Statistics*, John Wiley, Chichester, U. K.

Nichols, J. D., J. T. Clarke, S. W. H. Cowley, J. Duval, A. J. Farmer, J.-C. Gérard, D. Grodent, and S. Wannawichian (2008), Oscillation of Saturn's southern auroral oval, *J. Geophys. Res.*, *113*, A11205, doi:10.1029/2008JA013444.

Nichols, J. D., B. Cecconi, J. T. Clarke, S. W. H. Cowley, J.-C. Gérard, A. Grocott, D. Grodent, L. Lamy, and P. Zarka (2010a), Variation of Saturn's UV aurora with SKR phase, *Geophys. Res. Lett.*, *37*, L15102, doi:10.1029/2010GL044057.

Nichols, J. D., S. W. H. Cowley, and L. Lamy (2010b), Dawn-dusk oscillation of Saturn's conjugate auroral ovals, *Geophys. Res. Lett.*, *37*, L24102, doi:10.1029/2010GL045818.

Provan, G., D. J. Andrews, C. S. Arridge, S. W. H. Cowley, S. E. Milan, M. K. Dougherty, and D. M. Wright (2009a), Polarization and phase of planetary period oscillations on high latitude field lines in Saturn's magnetosphere, *J. Geophys. Res.*, *114*, A02225, doi:10.1029/2008JA013782.

Provan, G., S. W. H. Cowley, and J. D. Nichols (2009b), Phase relation of oscillations near the planetary period of Saturn's auroral oval and the equatorial magnetospheric magnetic field, *J. Geophys. Res.*, *114*, A04205, doi:10.1029/2008JA013988.

Provan, G., D. J. Andrews, B. Cecconi, S. W. H. Cowley, M. K. Dougherty, L. Lamy, and P. Zarka (2011), Magnetospheric period magnetic field oscillations at Saturn: Equatorial phase "jitter" produced by superposition of southern- and northern-period oscillations, *J. Geophys. Res.*, *116*, A04225, doi:10.1029/2010JA016213.

Provan, G., D. J. Andrews, C. S. Arridge, A. J. Coates, S. W. H. Cowley, G. Cox, M. K. Dougherty, and C. M. Jackman (2012), Dual periodicities in planetary-period magnetic field oscillations in Saturn's tail, *J. Geophys. Res.*, *117*, A01209, doi:10.1029/2011JA017104.

Provan, G., S. W. H. Cowley, J. Sandhu, D. J. Andrews, and M. K. Dougherty (2013), Planetary period magnetic field oscillations in Saturn's magnetosphere: Post-equinox abrupt non-monotonic transitions to northern system dominance, *J. Geophys. Res. Space Physics*, *118*, 3243–3264, doi:10.1002/jgra.50186.

Sandel, B. R., and A. L. Broadfoot (1981), Morphology of Saturn's aurora, *Nature*, *292*, 679–682.

Sandel, B. R., et al. (1982), Extreme ultraviolet observations from the Voyager 2 encounter with Saturn, *Science*, *215*, 548–553.

Southwood, D. J. (2011), Direct evidence of differences in magnetic rotation rate between Saturn's northern and southern polar regions, *J. Geophys. Res.*, *116*, A01201, doi:10.1029/2010JA016070.

Southwood, D. J., and M. G. Kivelson (2007), Saturn magnetospheric dynamics: Elucidation of a camshaft model, *J. Geophys. Res.*, *112*, A12222, doi:10.1029/2007JA012254.

Southwood, D. J., and M. G. Kivelson (2009), The source of Saturn's periodic radio emission, *J. Geophys. Res.*, *114*, A09201, doi:10.1029/2008JA013800.

Southwood, D. J., and S. W. H. Cowley (2014), The origin of Saturn's magnetic periodicities: Northern and southern current systems, *J. Geophys. Res. Space Physics*, *119*, 1563–1571, doi:10.1002/2013JA019632.

Wang, Z., D. A. Gurnett, G. Fischer, S.-Y. Ye, W. S. Kurth, D. G. Mitchell, J. S. Leisner, and C. T. Russell (2010), Cassini observations of narrowband radio emissions in Saturn's magnetosphere, *J. Geophys. Res.*, *115*, A06213, doi:10.1029/2009JA014847.

Warwick, J. W., et al. (1981), Planetary radio astronomy observations from Voyager-1 near Saturn, *Science*, *212*, 239–243.

Warwick, J. W., D. S. Evans, J. H. Romig, J. K. Alexander, M. D. Desch, M. L. Kaiser, M. Aubier, Y. Leblanc, A. Lecacheux, and B. M. Pedersen (1982), Planetary radio astronomy observations from Voyager-2 near Saturn, *Science*, *215*, 582–587.

Ye, S.-Y., D. A. Gurnett, J. B. Groene, Z. Wang, and W. S. Kurth (2010), Dual periodicities in the rotational modulation of Saturn narrowband emissions, *J. Geophys. Res.*, *115*, A12258, doi:10.1029/2010JA015780.

Zarka, P. (1998), Auroral radio emissions at the outer planets: Observations and theories, *J. Geophys. Res.*, *103*(E9), 20,159–20,194.

Zarka, P., L. Lamy, B. Cecconi, R. Prangé, and H. O. Rucker (2007), Modulation of Saturn's radio clock by solar wind speed, *Nature*, *450*, 265–267, doi:10.1038/nature06237.